The 13 January 2001 El Salvador earthquake: A multidata analysis

Martin Vallée and Michel Bouchon

Laboratoire de Géophysique Interne et Tectonophysique, Observatoire de Grenoble, Université Joseph Fourier, Grenoble, France

Susan Y. Schwartz

Earth Sciences Department and Institute for Geophysics and Planetary Physics, University of California, Santa Cruz, California, USA

Received 11 April 2002; revised 23 August 2002; accepted 2 January 2003; published 17 April 2003.

[1] On 13 January 2001, a large normal faulting intermediate depth event (M_w = 7.7) occurred 40 km off the El Salvadorian coast (Central America). We analyze this earthquake using teleseismic, regional, and local data. We first build a kinematic source model by simultaneously inverting *P* and *SH* displacement waveforms and source time functions derived from surface waves using an empirical Green's function analysis. In an attempt to discriminate between the two nodal planes (30° trenchward dipping and 60° landward dipping), we perform identical inversions using both possible fault planes. After relocating the hypocentral depth at 54 km, we retrieve the kinematic features of the rupture using a combination of the Neighborhood algorithm of *Sambridge* [1999] and the Simplex method allowing for variable rupture velocity and slip. We find updip rupture propagation yielding a centroid depth around 47 km for both assumed fault planes with a larger variance reduction obtained using the 60° landward dipping nodal plane. We test the two possible fault models using regional broadband data and near-field accelerograms provided by *Universidad Centro Americana* [2001]. Near-field data confirm that the steeper landward dipping nodal plane is preferred. Rupture propagated mostly updip and to the northwest, resulting in a main moment release zone of approximately 25 km × 50 km with an average slip of ~3.5 m. The large slip occurs near the interplate interface at a location where the slab steepens dip significantly. The occurrence of this event is well-explained by bending of the subducting plate. *INDEX TERMS:* 7209 Seismology: Earthquake dynamics and mechanics; 7203 Seismology: Body wave propagation; 7215 Seismology: Earthquake parameters; 7230 Seismology: Seismicity and seismotectonics; 7255 Seismology: Surface waves and free oscillations; *KEYWORDS:* El Salvador, source kinematics, subduction zone, neighborhood algorithm, inversion, empirical Green function

Citation: Vallée, M., M. Bouchon, and S. Y. Schwartz, The 13 January 2001 El Salvador earthquake: A multidata analysis, *J. Geophys. Res.*, *108*(B4), 2203, doi:10.1029/2002JB001922, 2003.

1. Introduction

[2] A large (M_w = 7.7) earthquake occurred at a depth of ~50 km within the subducting Cocos plate, 40 km off the El Salvadorian coast on 13 January 2001. This earthquake caused a lot of damage, mainly because of landslides triggered by the main shock. According to the Comite de Emergencia Nacional (COEN), 944 people were killed including 300 in the Las Colinas landslide in the neighborhood of Santa Tecla. The number of deaths might have been even greater if the event had occurred during the wet season when landslides are more easily triggered. A detailed report of this earthquake as well as the following shallow inland M = 6.6 earthquake (13 February 2001) is given by *Bommer et al.* [2002]. Large intraplate earthquakes in subduction zones are quite common although very few have reached the magnitude of the January 2001 earthquake. In El Salvador, the largest earthquake over the past century was a M_w = 7.2 intraslab normal event that occurred in 1982 at a location very close to the 2001 event. Yet an understanding of both the stresses that generate these events and the mechanics of their occurrence are poorly understood.

[3] The 2001 El Salvador earthquake was a normal faulting event with both nodal planes striking parallel to the coast with one dipping 55–60° to the northeast, toward Central America, and the other dipping ~30° to the southwest, toward the Pacific Ocean. The location of the aftershocks, concentrated landward and down dip of the main shock, suggests a preference for the steeper dipping plane (Figure 1), but this is not definitive. For many tensional intermediate depth events in slabs, the steeper of the two nodal planes has been assumed to be the fault plane (e.g., the 1950 northern Chile event [*Kausel and Campos*, 1992] or the 1999 Oaxaca, Mexico, earthquake [*Singh et al.*, 2000]). Yet, when a careful seismological analysis is conducted, for example, with aftershock relocations, results

0148-0227/03/2002JB001922$09.00

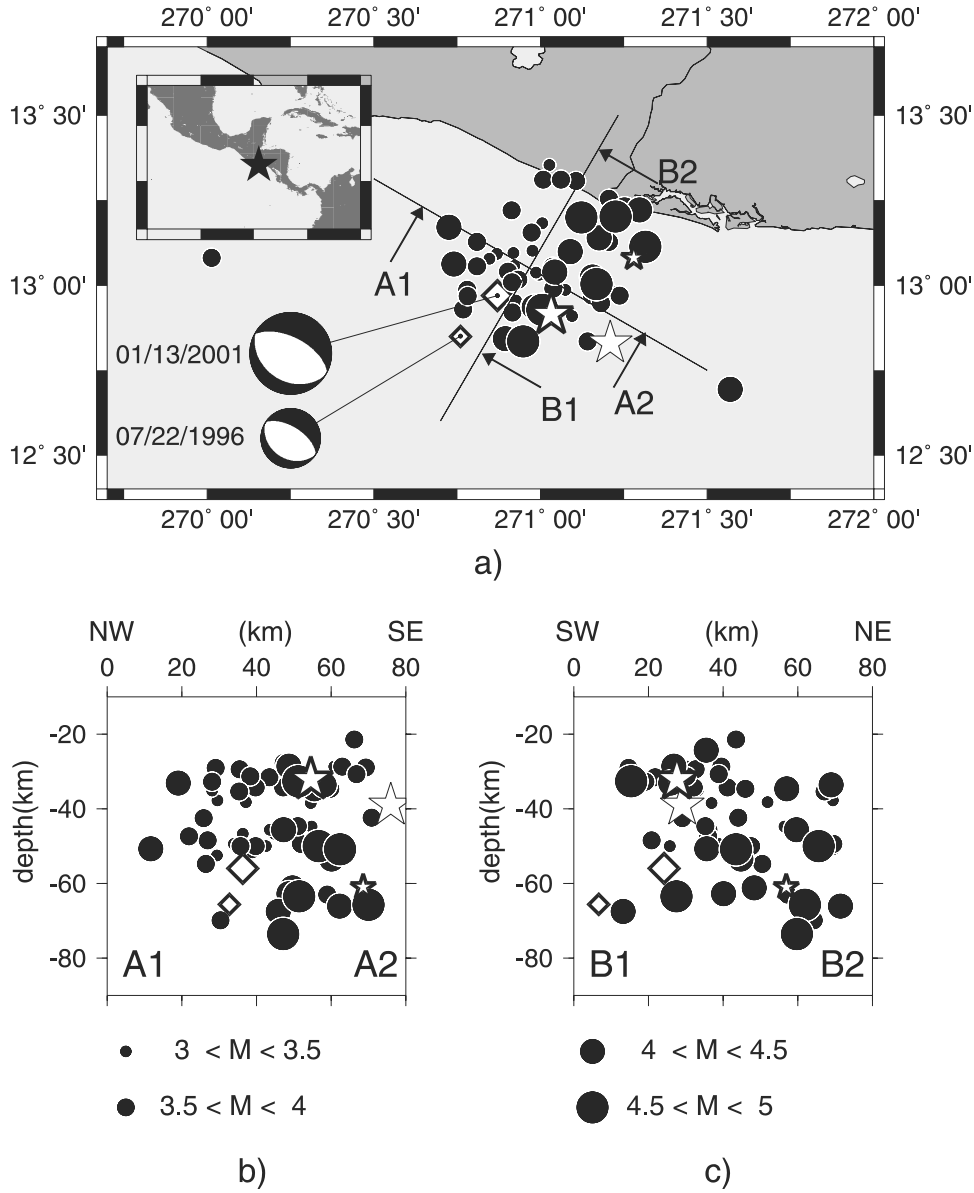

Figure 1. Location of the main shock and its aftershocks occurring within 10 days of the event determined by Centro de Investigaciones Geotecnicas (CIG), El Salvador in (a) map view and (b) cross section along A1–A2, and (c) B1–B2. The large thick star gives the regional hypocentral location of the main shock from CIG, while the large thin star gives the USGS location of the main shock. The small black star shows the USGS location of the EGF. The focal mechanism determined in this study (slightly modified from the Harvard CMT solution) and the Harvard CMT solution for the EGF are also indicated. The large and small diamonds represent the Harvard CMT locations of the main shock and of the EGF, respectively.

have varied. For instance, *Ratchkovski and Hansen* [2001] identify the subvertical nodal plane as the fault plane for events of the 1999–2000 Kodiak Island, Alaska, sequence, while the subhorizontal nodal plane was favored by *Takeo et al.* [1993] for the 1993 Kushiro-Oki, Japan, event. *Hernandez et al.* [2001] tested both nodal planes using near-field data for the 1999 Oaxaca, Mexico, event and found only a very slight preference for the steeper plane. *Cocco et al.* [1997], studying the Zihuatanejo, Mexico, event (10 December 1994, M_w = 6.6), also favored the steeper plane from a subevent analysis but could not completely reject the conjugate plane. In this respect, the very large M_w = 8.0 1977 Tonga event has been very controversial: *Christensen and Lay* [1988] argued that the two planes could not be discriminated due to the very small vertical extent of the rupture, while *Lundgren and Okal* [1988] concluded that the actual fault plane was the steeper one after having identified both a deeper subevent and a deeper centroid. Determination of the fault plane for intermediate depth slab events is important as it may help to discriminate between several proposed mechanisms for their generation.

[4] Both static and dynamic mechanisms have been proposed to explain the occurrence of large intraplate earthquakes at subduction zones. Stresses induced by the sub-

duction process including sinking, flexure, warping, or tearing of the slab, as well as its thermal equilibration have all been attributed to earthquake generation at intermediate depth within subducting lithosphere. Bending stresses, as slabs plunge into the mantle, have been identified as the principle cause of outer rise earthquake activity, where a neutral surface separates tensional outer rise events at shallow depth from compressional events deeper within the slab. A few very large tensional outer rise events, such as the 1977 Sumba (M_w = 8.2) and the 1931 Sanriku (M_w = 8.3) earthquakes, where rupture appears to have propagated through the entire lithosphere, require an alternative explanation. Enhanced gravitational effects of the sinking slab (slab pull) at relatively weakly coupled subduction zones have been attributed to rupture of the entire oceanic lithosphere during these events (e.g., *Lynnes and Lay* [1988] or *Given and Kanamori* [1980]).

[5] Dynamic mechanisms to explain intraplate earthquakes at subduction zones have also been proposed. *Astiz and Kanamori* [1986], *Christensen and Ruff* [1988], and *Lay et al.* [1989] all provide evidence, from focal mechanisms of intraplate events, for temporal variations in subduction zone stresses that are related to large underthrusting events on the plate interface. These studies have found that in coupled subduction zones, tensional faulting events in the outer rise and at intermediate depth tend to follow and precede large underthrusting events, respectively, while compressional events in the outer rise and at intermediate depth tend to precede and follow the great thrust events respectively. *Dmowska and Lovison* [1992] found that moderate to large earthquakes at intermediate depth in slabs tend to concentrate near the down dip edge of the coupled plate interface where the locked plate boundary causes stress concentrations in adjacent regions. Examples of intraslab earthquakes that occur just below the down dip edge of a coupled plate interface include the 1931 (M = 7.8) and 1999 (M_w = 7.5) Oaxaca, Mexico [*Singh et al.*, 2000; *Mikumo et al.*, 2002]; the 1994 (M_w = 6.6) and 1997 (M_w = 7.3) Michoacan, Mexico [*Cocco et al.*, 1997; *Mikumo et al.*, 1999]; the 1999 (M_w = 7) and 2000 (M_w = 6.5) Kodiak Island [*Ratchkovski and Hansen*, 2001]; and the 1982 (M_w = 7.2) and 2001 (M_w = 7.7) El Salvador events. These dynamic models for intraplate events open the possibility that both the 1982 and 2001 tensional, intermediate depth El Salvador events are heralding the occurrence of a large underthrusting event in this region and identifying the moment release locations for this future earthquake. Yet, in the Oaxaca, Michoacan, and Kodiak Island cases, large underthrusting earthquakes are well documented with the last events occurring in Oaxaca in 1978, in Michoacan in 1985, and in Alaska in 1964. The El Salvador segment of the Middle American Trench has not experienced a great underthrusting earthquake in the twentieth century. Therefore it may be weakly coupled and more relevant to compare it with the Tonga subduction zone where the largest known intermediate depth tensional event occurred (M_w = 8 on 22 June 1977) and where very large underthrusting events are rare. In this case, dynamic interactions would not be expected to strongly influence the seismicity of the region and static mechanisms described before would dominate.

[6] We investigate the source process of the 2001 event to determine which of the two nodal planes is the fault plane and the slip and rupture velocity distributions on that plane. In a first stage, we attempt to do so with teleseismic data alone and will find that there is only a moderate distinction between the two planes. This is why, in a second stage, we add regional and local data sets to further help us discriminate between the two planes. Incorporating various data allows us to test the consistency between teleseismic, regional, and near-field data. Our results will be used to assess possible models for the generation of this event.

2. Modeling of Teleseismic Waveforms

[7] We first determine the best event depth and focal mechanism and then use these in a simultaneous inversion of body and surface wave data to retrieve the kinematic parameters of the rupture. *P* and *SH* displacement waveforms are combined with source time functions, obtained from an empirical Green function analysis of surface waves, to solve for the slip distribution on both possible nodal planes. The following sections describe (1) determination of the main characteristics of the event (depth and focal mechanism), (2) data used in the inversion for kinematic source parameters, (3) methods used to extract kinematic source parameters from the data, (4) model parameterization, (5) inversion method, and (6) the results.

2.1. Main Earthquake Characteristics

[8] Before retrieving details of the rupture, the event hypocentral depth and focal mechanism must be carefully determined. Table 1 lists values of hypocentral depth, strike, dip, and rake obtained for this event by various groups. Depths range between 32 km (regional data from Centro de Investigaciones Geotecnicas, CIG) and 56 km (Harvard centroid moment tensor (CMT)). To determine the best event depth to use in our source modeling, we use a smaller event (M_w = 5.6), which occurred on 22 July 1996 at nearly the same location (Figure 1), as a reference event to relocate the hypocentral parameters of the main shock. The main advantage of the reference event is that its *pP* phase is very clear at many teleseismic stations. Moreover, its small size allows us to assume that the *pP* time is controlled by its hypocentral depth. Figure 2a shows observed *pP* times for the reference event at several stations in North America along with calculated values using the crustal model listed in Table 2 [*Kim et al.* 1982]). The best fit to the *pP* times is obtained for an hypocentral depth of 64 km.

[9] Table 3 indicates the arrival time differences between the two events observed at common stations at different distances and azimuths (the station PTGA is chosen as a reference station). Arrivals from the reference event are often noisy at South American stations, and therefore few values come from this azimuthal range (southeast). The very small time shifts indicate that both events are located close to one other. We inverted these time shifts using takeoff angles from *Pho and Behe* [1972], a source *P* wave velocity of 8 km s^{-1}, and a grid search algorithm to obtain the spatial and temporal offset between events (δx, δy, δz, δt). Figure 2b shows the variance reduction obtained as a function of the depth difference. The best fit is obtained for a main shock hypocenter lying 10–15 km above the reference event. The corresponding values of δx, δy, and δt are 3 km south, 14 km east, and 0.436 s from the reference event, respectively. We

Table 1. Earthquake Parameters for the EGF and Main Shock (MS) Determined by Different Agencies and in This Study[a]

	MS HRV	MS USGS	MS ERI	MS (CIG)	MS (this study)	EGF HRV
Longitude, deg	−89.13	−88.79	nd	−88.97	nd	−89.24
Latitude, deg	12.97	12.83	nd	12.91	nd	12.85
Strike 1, deg	121	149	nd	nd	119	125
Dip 1, deg	35	45	nd	nd	31	31
Rake 1, deg	−95	−73	nd	nd	−88	−88
Strike 2, deg	307	306	315	nd	297	302
Dip 2, deg	56	48	61	nd	58	59
Rake 2, deg	−86	−107	−103	nd	−93	−91
Depth, km	56.	39.	50.	32.	48.	65.5
M_w	7.7	7.6	7.6	nd	7.7	5.6

[a]Sources are CIG, Centro de Investigaciones Geotecnicas, El Salvador; ERI, Earthquake Research Institute, Japan; HRV, Harvard University, United States; USGS, U.S. Geological Survey, United States; nd indicates that institutions have not given information on the considered earthquake parameters.

therefore adopt an hypocentral depth of 49–54 km for the main shock, deeper then the values determined by CIG (32 km) and U.S. Geological Survey (USGS) (39 km).

[10] The Harvard CMT focal mechanism fits the *SH* waves from near nodal stations poorly, particularly, the *SH* displacement at station SFJ (which is very weak, see Figure 5 below). We therefore modified this solution and obtained a superior fit to all *P* and *SH* data with the mechanism indicated in Table 1.

2.2. Data Used in the Teleseismic Analysis

2.2.1. Body Waves

[11] We used 16 *P* and 8 *SH* waveforms provided by the IRIS and Geoscope networks. These stations are at epicentral distances ranging between 35° and 80° so that mantle propagation is simple to model. The azimuthal distribution (Figure 3) is satisfactory although denser on the northern side of the event. Additional stations exist at northern azimuths, but their inclusion may bias the inversion results without assigning differential weighting which is often difficult to determine. *Ihmle* [1998] showed the high consistency of the body waves in his study of the 1994 Bolivia earthquake; by modeling only 10 stations, well distributed around the event, he reproduced the waveforms at stations not included in the inversion.

[12] The first 60 s of the vertical *P* and transverse *SH* displacements obtained through direct integration of the broadband velocity records, which include the direct source radiation and its crustal and free surface reflections, were selected. Although *SH* waves are often noisier and have lower frequency content than *P* waves, they are important in constraining the focal mechanism and have more sensitivity to directivity effects because of their lower phase velocities.

2.2.2. Surface Waves

[13] Surface waves are very sensitive to horizontal directivity because of their low phase velocities and can therefore provide important constraints on the lateral extent of the rupture. Nevertheless, unlike body waves, knowledge of the Earth's interior is not good enough to allow high-frequency modeling of these waves. Direct use of long-period surface waves for source inversion, usually does not allow for more than a point source characterization, except for very large events ($M > 7.5–8$). For this reason we use an empirical Green function (EGF) approach and will combine information from this analysis with *P* and *SH* displacement waveforms in our source parameter inversion. We use the same

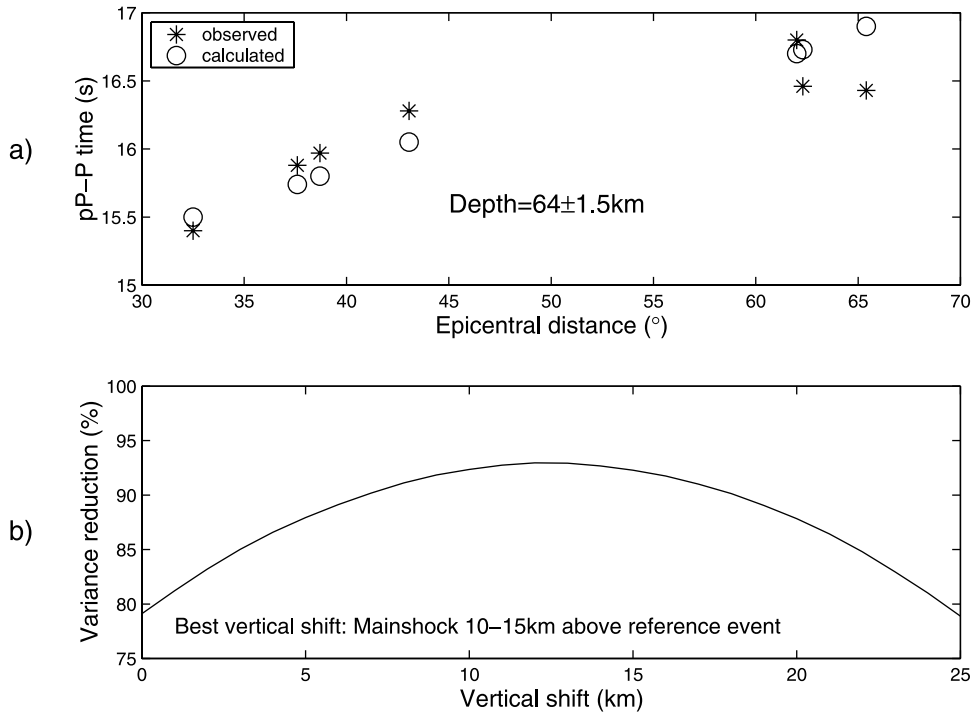

Figure 2. Relocation analysis of the main shock relative to a small reference event. (a) A depth of 64 km is obtained for the reference event by modeling the *pP-P* times at stations located at different distances. (b) A main shock depth between 10 and 15 km shallower than the reference event provides the largest variance reduction for time shifts between the two events.

Table 2. Local Source Crustal Structure[a]

Thickness, m	V_P, m s^{-1}	V_S, m s^{-1}	ρ, kg m^{-3}	Q_P	Q_S
9600	5690	3285	2650	400	200
14600	6140	3545	2800	500	200
13200	6800	3926	2900	400	200
0	8000	4619	3300	800	400

[a]From *Kim et al.* [1982].

M_w = 5.6 reference event used to relocate the main shock as the EGF (Figure 1). This event is the only one which meets all the requirements of an EGF: similar location, focal mechanism and depth, much smaller magnitude, and therefore source duration compared with the main shock, and it is recorded by many stations in common with the main shock. We selected eight stations which recorded both events and have good signal to noise for the small EGF (Figure 4). These stations are all <50° from the source area but have a good distribution in the "directivity parameter" Γ (Γ = cos(θ)/v_ϕ) where θ is the station azimuth and v_ϕ is the phase velocity of the selected wave). The similarity of the waveforms from both events is illustrated in Figure 4 by the recordings at station FFC. This provides confidence in the suitability of the EGF chosen in this study.

[14] Good descriptions and applications of the EGF analysis are given by *Velasco et al.* [1994a], *Courboulex et al.* [1997], and *Schwartz* [1999]. Theoretically, the method provides direct access to the relative source time functions (RSTFs) by simply deconvolving, at different stations, the EGF from the main event. Therefore the main advantage of the method is that no assumption is made about the propagation between the source and the receiver. Nevertheless, we can only obtain the low-frequency source time function because no details above, or of the order of, the corner frequency of the EGF can be retrieved. Moreover, if the medium is strongly laterally heterogeneous at the source or if the rupture has a large vertical extent, this method becomes more questionable because different Green functions should be used depending on the position of the rupture. Another limitation arises due to the difference in location between the main shock and the EGF; even if the EGF is very close to the main shock, the finite rupture extent of the main shock may prevent the high-frequency details of the rupture from being retrieved. *Velasco et al.* [1994b] tested quantitatively the influence of the position of the EGF for different rupture lengths. Their results show that for a 25 km long rupture, periods down to 10 s are really reliable when the EGF and the main shock centroid are separated by 10–20 km. For a 100 km long rupture, it is more appropriate to use periods only above 20 s. For the El Salvador earthquake, with a rupture length on the order of 25 km (which will be confirmed by the inversion results), our results should contain information at periods down to 10 s.

Table 3. Observed Time Shifts Between the Main Shock and the Reference Event Used in the Relative Relocation Analysis[a]

Station	Azimuth, deg	Takeoff Angle, deg	Time Shift, s
UNM	304.00	89.99	2.00
PFO	314.11	39.75	2.42
BKS	315.70	37.60	2.58
TUC	317.58	40.76	2.44
CMB	317.61	38.15	2.62
ANMO	327.09	40.86	2.51
COLA	336.30	28.30	2.47
INK	342.86	29.27	2.00
FFC	348.90	36.56	2.18
RES	358.00	29.42	1.80
SSPA	17.30	40.63	1.72
DRLN	29.15	35.84	1.08
SJG	73.00	48.28	0.50
PTGA	113.25	40.00	0.00
NNA	153.84	40.86	1.10

[a]The time reference is defined by the station PTGA.

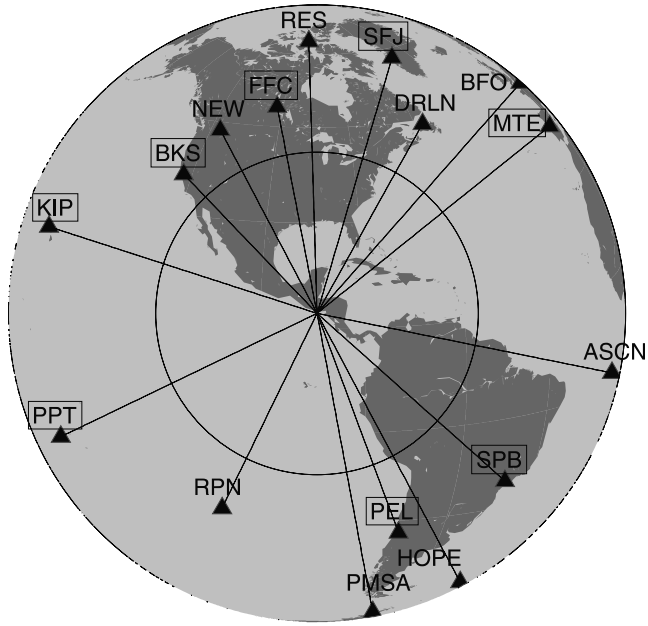

Figure 3. Location of teleseismic stations used in the body wave inversion. Framed stations are those from which both *P* and *SH* waves are used.

[15] Because of the very good similarity between the EGF and the main shock, the deconvolution is performed directly in the frequency domain, without using the usual "water level technique." We consider only Rayleigh waves which avoids the uncertainties related to the use of different phase velocities in the directivity parameter. Moreover, Love waves do not improve the directivity parameter distribution because of their higher phase velocities. We use the vertical components and isolate the Rayleigh wave using a phase velocity window between 4 and 2.3 km s^{-1} (indicated on Figure 4). Deconvolutions are stable, and the RSTFs are presented in Figure 5b. Lower-amplitude and longer-duration RSTFs at stations to the southeast compared to the north suggest northwest rupture directivity. This will be validated by our formal inversion for the kinematic source parameters described in the following sections.

2.3. Extended Source Forward Calculations

2.3.1. Body Wave Displacements

[16] In order to define the slip distribution on the fault and attempt to discriminate between the two possible fault planes, we modeled the earthquake as an extended source. In this model, the fault is discretized into subfaults and the kinematic parameters, onset time *T*, risetime *d*, and the amount of slip *s* are retrieved for each subfault [*Hartzell*

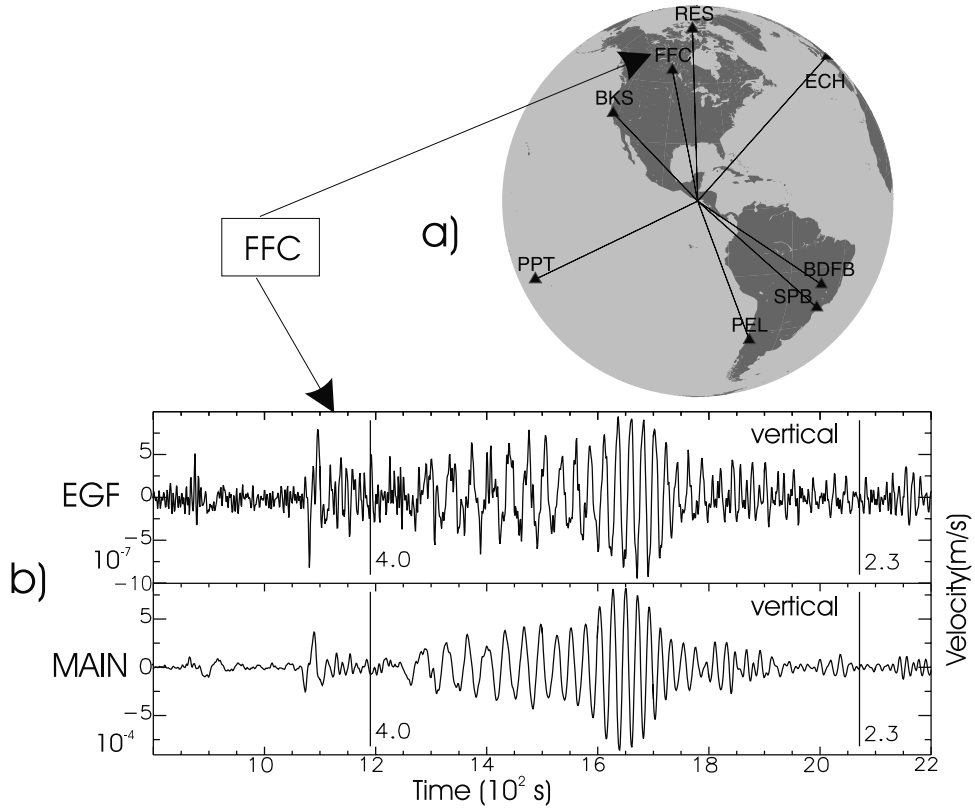

Figure 4. (a) Location of the stations used in the surface waves analysis. (b) Comparison of vertical component EGF and main shock waveforms at station FFC. Note the similarity in the waveforms and the 1000 times larger amplitude of the main shock. The time window used to isolate the Rayleigh waves for the deconvolution is defined by phase velocities between 2.3 and 4.0 km s^{-1} and is indicated on the seismograms.

and Heaton, 1983]. Each subfault is itself represented by an array of point sources which must be fine enough to mimic continuous rupture. The spectral displacement at a station is simply given by a sum over all the n point sources, with the appropriate time and space shift. This can be written [e.g., *Cotton and Campillo*, 1995]

$$U(\omega) = S\sum_{j=1}^{n} G(z_j)\mu_j \mathrm{TF}\left[\mathrm{Tr}(t, s_j, d_j)\right] e^{i(kl_j - \omega T_j)}, \qquad (1)$$

where

- $G(z_j)$ ground motion for a unit moment point source at a depth z_j with a given source mechanism;
- μ_j rigidity around the point source j;
- S surface modelled by one point source;
- $\mathrm{Tr}(t, s_j, d_j)$ assumed local source time function: triangle of width d_j and maximum amplitude $2s_j/d_j$;
- k horizontal wave number;
- l_j horizontal space shift between the hypocenter and point source j;
- TF Fourier transform.

$G(z)$ for both P and SH waves are computed using the reciprocal approach [*Bouchon*, 1976]. The source crust is represented by the one-dimensional crustal model of *Kim et al.* [1982] (Table 2). This model was obtained using wide-angle reflections between shallow earthquakes in Guatemala and a station in Honduras. It therefore gives a good estimation of the El Salvador crust. The recent study of *Walther et al.* [2000] in Nicaragua confirms a Moho depth around 40 km in this region. Although more refined velocity models taking into account dipping layers may be more appropriate to represent the complex structure around the source [*Wiens* 1989], such detailed information is not available, and we therefore use a simple one-dimensional model rather than a poorly constrained complex model. The more robust features should be relatively independent of precise knowledge of the velocity structure. Moreover, we consider that the different approaches used in this study and particularly use of the empirical Green function analysis will allow us to limit the errors caused by use of a simplified velocity structure. Receiver crustal structures are taken from the global study of *Mooney et al.* [1998], and thus the effect of different Moho depths below each station is included in this study. Attenuation in the mantle is taken into account through a t^* factor equal to 0.7 s for P waves and 2.8 s for S waves. Values derived from the PREM model would yield a t^* factor equal to 1 s for P waves, but this value seems too high, as documented by *Ekström* [1989].

2.3.2. Surface Wave Relative Source Time Functions

[17] The source time functions retrieved by the EGF method are not the absolute source time functions but the relative source time functions (RSTF) that depend on the

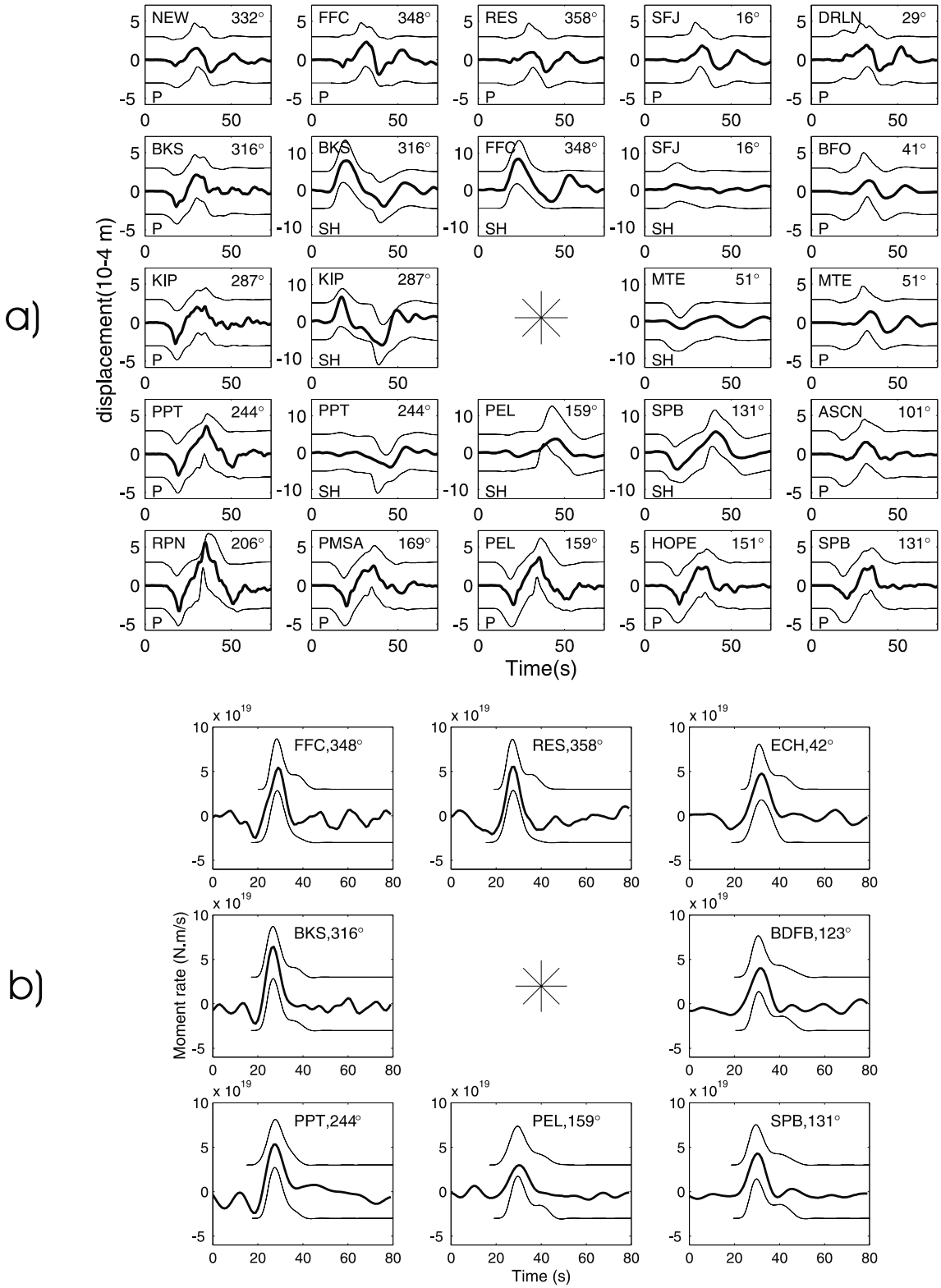

Figure 5. Preferred model fits to teleseismic data: the thick lines are the data, thin lines beneath the waveforms are obtained with the 60° dipping plane, while thin lines above the waveforms are obtained with the 30° dipping plane. The representations are approximately geographical and station azimuths are labeled in the upper right corner of the seismograms. (a) Comparison between actual and computed body wave displacements. The *P* waves are presented in the outer part and *SH* waves in the inner part. A different scale is used for *P* waves and *SH* waves. (b) Comparison between actual and computed apparent source time functions for Rayleigh waves. Computed source time functions are low-pass filtered at 10 s and the EGF magnitude is assumed to be 5.8.

azimuth θ of the station, the phase velocity v_ϕ at the source and the kinematic parameters of the source. If we denote $f(x, z, t)$ the local source time function at a point (x, z) on the fault, the RSTF noted $F_\theta(t)$ may be written

$$F_\theta(t) = \int\int_F f\left[x, z, t + D(\theta, x, z)/v_\phi\right] dx\, dz, \qquad (2)$$

where $D(\theta, x, z) = x\cos(\theta - \theta_F) + z\cot an(\delta_F)(\theta - \theta_F)$ and δ_F and θ_F are the dip and strike, respectively, of the fault F, which gives in the discrete case (subfault grid) with the assumed local source time function and the notations of equation (1):

$$F_\theta(t) = S\sum_{j=1}^{n} \mu_j \mathrm{Tr}\left(t - T_j + D_j/v_\phi, s_j, d_j\right). \qquad (3)$$

[18] The Rayleigh wave phase velocity is approximated to be 3.8 km s^{-1} according to *Schwartz* [1999]. As equation (1), equation (3) gives the forward relationship between kinematic parameters on the fault and observed data. Next, we describe the inverse problem to deduce the source parameters from our observations.

2.4. Model Parameterization

2.4.1. Grid Size

[19] We perform the source inversion using both possible nodal planes. Both fault planes are modeled using a 70 km × 70 km grid, positioned such that the 54 km deep hypocenter is located 30 km along strike of the southeast extremity and 30 km updip of the fault plane termination. This yields a depth extent between 20 and 80 km for the 60° dipping plane and between 33 and 69 km for the 30° dipping plane. These values were chosen to encompass the 10 day aftershock distribution which is assumed to represent the maximum rupture area (Figure 1). The size of the subfault grid has to be tuned to the resolving power of the data: if too fine a grid is used, the problem becomes highly nonunique because the high-frequency energy of the waveforms is very low. Moreover, the inverse problem becomes complicated due to the high number of unknowns. On the contrary, if the grid is too large, the solution may be unique but only the very large-scale details of the rupture can be retrieved. To avoid these difficulties, numerous studies [e.g, *Hartzell and Heaton*, 1983; *Mendoza et al.*, 1994] use a fine grid combined with a large smoothing parameter. In our case, this approach would necessitate the use of iterative gradient methods because of the high-dimensional, nonlinear nature of our problem (a completely free rupture velocity makes the inverse problem nonlinear). We prefer to solve for fewer parameters and employ semiglobal inversion methods. Thus we choose to use a relatively large subfault grid of 10 km × 10 km and only slight smoothing. Because the *P* wave velocity c is around 8 km s^{-1} in the source region, this grid size allows us to model frequencies up to 0.4 Hz ($f_{max} = c/\lambda_{min} = c/(2dx)$). The final discretization of the fault is done in an array of 7 × 7 subfaults themselves discretized in arrays of 4 × 4 point sources.

2.4.2. Kinematic Parameters

[20] Slip is retrieved for each subfault and is allowed to vary between 0 and 10 m but is constrained to go to zero on the borders of the fault. This is why we have oversized the dimension of the fault. To allow for variable rupture velocity, we use the finite difference scheme of *Podvin and Lecomte* [1991]. This algorithm, based on the local Fermat principle, was originally designed to compute arrival times in two- and three-dimensional models. Yet it can also be used to compute onset rupture times on a fault with variable rupture velocity. It has been used in this respect by *Herrero* [1994]. This algorithm naturally imposes rupture causality (i.e., one subfault cannot slip if the rupture front has not reached one of its neighbors). Moreover, the rupture velocity is a completely free parameter which is not the case with the time window approach introduced by *Hartzell and Heaton*, [1983]. In our case, possible rupture velocity values will range between 1000 and 4300 m s^{-1}, this last value representing $\sim 0.9V_s$ in the hypocentral region. Finally, we consider the local duration to be constant (this parameter is usually poorly resolved, [*Ihmle*, 1998] and equal to 2 s. Taking into account that the kinematic parameters are fixed on the borders of the fault, we will invert for a total of 72 parameters ((6 × 6) values for both the rupture velocity and the slip).

2.5. Inversion Method

[21] To retrieve the values of subfault slip and rupture velocity, we simultaneously minimize the L1 norm of the residuals between observed and calculated body wave displacements (using equation (1)) and the residuals between the widths of source time functions deconvolved from Rayleigh waves and calculated using equation (3). The body waves are sampled at 0.625 s and the first 38 and 58 s were inverted for *P* and *SH* waves, respectively. The width of the source time functions was estimated as the half peak value width, i.e., the time during which the moment rate function is above half of its maximum value. This is a more robust value to estimate than either the total duration of the source time functions or the time to attain the peak value since there is often a negative part, without any physical significance, at the beginning of the observed RSTFs (see Figure 5b). Another possibility would be to invert the peak value itself but this parameter is very dependent on the filtering used in the EGF determination of the source time functions.

[22] The L1 norm was shown by *Ihmle* [1998] to be superior in fitting small details in the waveforms. Although the L2 norm is much more often used, *Hartzell et al.* [1991] have shown that both norms have advantages and that the robustness of the L1 norm is useful to avoid overweighting a single bad data point.

[23] To solve this inverse problem, we combined a method called Neighborhood Algorithm (NA) [*Sambridge*, 1999] with the Simplex method [*Nelder and Mead*, 1965]. This procedure can be compared to the one used by *Hartzell and Liu* [1996]. NA is a method which belongs to the same class of algorithms as simulated annealing or genetic algorithms and is therefore well adapted to nonlinear multiparameter problems. The main strategy of the method is to remain exploratory throughout the convergence process to reduce the risk of being trapped by a local minimum. As shown by *Sambridge* [1999], this method is even more exploratory than genetic algorithm or simulated annealing, which are generally exploratory only at the beginning of the process. *Lomax and Snieder* [1994] also pointed out the difficulty of turning the genetic algorithm into a fully exploratory algorithm. One advantage of NA over genetic

algorithm is that it requires the definition of only two tuning parameters which makes this algorithm easier to use. The idea behind NA is to decompose the parameter space in Voronoi or "neighborhood" cells and to identify, more and more precisely, throughout the process the location of the "good" cells. More details of NA are fully explained by *Sambridge* [1999]. Applications to source studies are also given by *Kennett et al.* [2000] and *Marson-Pidgeon et al.* [2000]. The two tuning parameters, called n_s and n_r, describe the number of models tested at each iteration and the number of the best fit cells, respectively, that will be considered at the following iteration to define the n_s new models. In our case, NA was used with $n_s = 30$, $n_r = 4$ and a total number of iterations of 1500. These parameters represent a trade-off between too exploratory a scheme, which would never converge on an acceptable model, and too directed a search, which would probably lead to a local minimum.

[24] Nevertheless, particularly in high-dimensional inverse problems (here the number of parameters is $n_d = 72$), NA cannot be used directly to deduce the best model. As a matter of fact, its goal is to identify possible models and not to converge toward one best model. This is why we use the $(n_d + 1)$ best models found by NA as starting points for the Simplex method. Contrary to NA, which is a sampling algorithm, Simplex is an optimization algorithm. These types of algorithms (like gradient methods) are very dependent on the starting model, and this is why it is necessary to use these methods with good starting values. We validate the stability of our final solution by using the Simplex method on a variety of starting models generated with NA. This approach allows us to estimate the standard errors of our results by using the marginal distributions in the same way as *Ihmle* [1998].

2.6. Source Process Inferred by the Combined Use of Body and Surface Waves

[25] For each of the possible fault planes 20 runs of the inversion method, with different values of the smoothing parameter and the relative weight between body and surface waves, were performed. In Figures 6 and 7 we show the results of this analysis. In Figure 6, we first present our preferred models, for both the slip and the rupture velocity. Then, in Figure 7, on the basis of the marginal distributions of the 20 tested models, we present the mean models and the standard errors. The mean model is not chosen as our preferred model because it induces a too smooth source process.

[26] Waveforms corresponding to the preferred models are presented in Figure 5a for body waves and Figure 5b for surface waves. Displacements presented in Figure 5a are not filtered; however, the computed apparent source time functions are low-pass filtered at 10 s according to the intrinsic high-frequency limitation of the EGF analysis. The fit of our preferred models is better for the 60° dipping plane with a variance reduction of 75.4% for *P* waves and 53.7% for *SH* waves compared to 65.8% and 53.7%, respectively, for the 30° dipping plane. Note that the lower variance reduction obtained for *SH* waves is partly due to the inclusion of station PEL: the fit for *SH* waves would be 60.9% and 61.4% if we did not use this station. The fit for surface waves is more difficult to estimate in terms of variance reduction since we only compare the pulse widths and it is difficult to estimate the prior variance of this parameter. Yet the direct comparison of misfit with the L1 norm also gives a better fit for the 60° dipping plane: $\Sigma|\text{width}_{\text{calc}} - \text{width}_{\text{obs}}| = 3.2$ s for the 60° dipping plane and 6.5 s for the 30° dipping plane.

[27] Some rupture characteristics are common for the two fault plane models: both yield similar moments of 4.8×10^{20} N m, rupture surfaces consisting principally of a single patch with a dimension of approximately 50 km × 25 km, similar rupture velocity distribution and mainly updip rupture propagation. This last characteristic is necessary to explain the impulsive reflected *P* phases (see for example RPN, PPT, or PEL in Figure 5a). More efficient updip directivity for the steeper dipping plane is precisely one of the reasons that the 60° dipping plane fits the data better. This fault plane model yields a maximum slip around 6 m and a centroid depth at 47 km. It also shows northwesterly rupture propagation, needed to explain the impulsive *P* wave at KIP compared with SPB (given the focal mechanism, the waveforms at these stations would be identical for a symmetric rupture) and the higher-amplitude shorter-duration source time functions at BKS compared with PEL and SPB (Figures 5a and 5b). Slip values are better resolved for the 60° dipping plane as can be seen by the standard errors in Figure 7. Slip standard errors average around 0.6m for this plane with an extremal value of 1.2 m.

[28] Rupture velocities, although completely free to range between 1 and 4.3 km s^{-1} at the beginning of the inversion process, cluster around 3.2 km s^{-1} over the majority of the fault plane. In the 60° dipping plane model, this value is quite well resolved, as can be seen by the standard errors in the zone updip of the hypocenter: a typical value is 200 m s^{-1}. For the 30° dipping plane, the standard errors are significantly higher. The rupture velocity obtained represents approximately 0.7 to $0.8V_s$ depending on the position of the rupture compared to the 37 km deep Moho in our crustal model, thus it seems to be a classical sub-Rayleigh phase velocity value. Because we do not smooth the rupture velocity (we slightly smooth the slip which can have an indirect effect), our results indicate a smooth, circular rupture front propagating over the fault plane with a rupture duration of 13 s, relatively short for such a large event. Simpler and shorter source time functions with increasing depth have been observed for interplate [*Bilek and Lay*, 1998] events and also for global seismicity [*Houston*, 2001].

[29] The area of main moment release for this earthquake is concentrated near the hypocenter and is small for an event of this size, which partly explains why it is so difficult to discriminate between the two possible nodal planes. An illustration of this characteristic is given by the relatively high value of the stress drop. In the case of a circular fault of radius r and average dislocation *D*, the stress drop is given by [*Eshelby*, 1957]

$$\Delta\sigma = 7\pi\mu D/(16r). \tag{4}$$

Replacing $\mu D\pi r^2$ by the moment M_w, equation (4) can be written

$$\Delta\sigma = 7M_w/(16r^3). \tag{5}$$

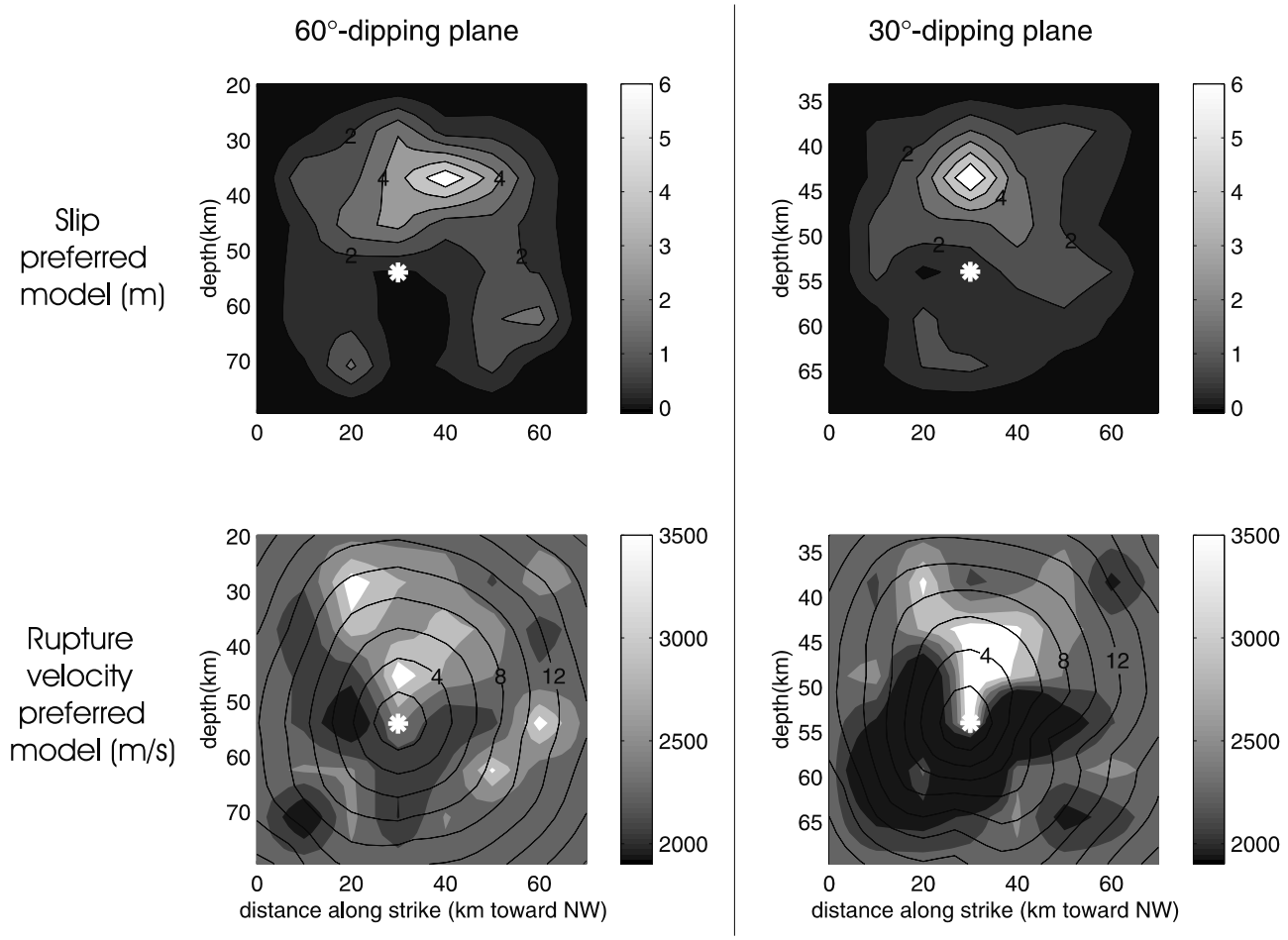

Figure 6. Preferred rupture models obtained with the extended source analysis. The hypocenter is denoted by the star. (top) Slip and (bottom) rupture velocity for (left) 60° dipping plane and (right) 30° dipping plane. Slip is contoured every 1 m, and rupture velocity is contoured every 300 m s^{-1}. Isochrons of the onset time are superimposed on the rupture velocity distributions.

Approximating the earthquake source as a circular rupture of source radius r equal to 25 km (also consistent with the aftershock area, Figure 1), relation (5) yields $\Delta\sigma = 130$ bars for the 60° dipping plane. This value is high compared with other intraplate events. Among 21 events of seismic moment larger than 5×10^{19} N m, *Kanamori and Anderson* [1975] found none with a stress drop higher than 100 bars. Other studies based on more recent earthquakes have confirmed this observation. The El Salvador earthquake has a higher stress drop than the intraplate events analyzed by *Scholz et al.* [1986] and very few intraplate events analyzed by *Mohammadioun and Serva* [2001], on the basis of the work of *Wells and Coppersmith* [1994], have stress drops above 100 bars.

[30] Finally, as an illustration of the utility of the combining body and surface waves in a combined inversion we present results obtained using body waves alone. For each of the possible fault planes 10 runs of the inversion method using two different smoothing parameters were performed. The mean models and the standard errors, for both the slip and the rupture velocity, are presented in Figure 8. These models lead to a variance reduction of 78% and 70% for *P* waves and 60% and 57% for *SH* waves for the 60° and 30° dipping planes, respectively. The fit is slightly better than body and surface waves combined. The models have noticable differences; the 60° fault plane body wave solution has the main moment release zone extending farther to the northwest. This model is close to the *Earthquake Research Institute* (*ERI*) [2001] model, which was determined with *P* waves alone. This northwest extension of the rupture is inhibited in the combined inversion due to the lack of northwest directivity observed in the surface waves. The rupture velocity is much more scattered than in the combined inversion (both the mean models and the standard errors are more variable). This is expected because the surface waves phase velocity is much closer to the rupture velocity, therefore allowing surface waves to better constrain this parameter.

3. Validation With Other Data

[31] In this section, we test our best teleseismically determined rupture models obtained for both nodal planes against regional and local data sets. The better fit to the teleseismic data for the steeper dipping nodal plane is moderate and additional data is required if we hope to discriminate between these two fault planes. Moreover, we have made various assumptions in the extended source analysis (crustal source structure, subfault size, constant duration, smoothing parameter, etc.), and therefore valida-

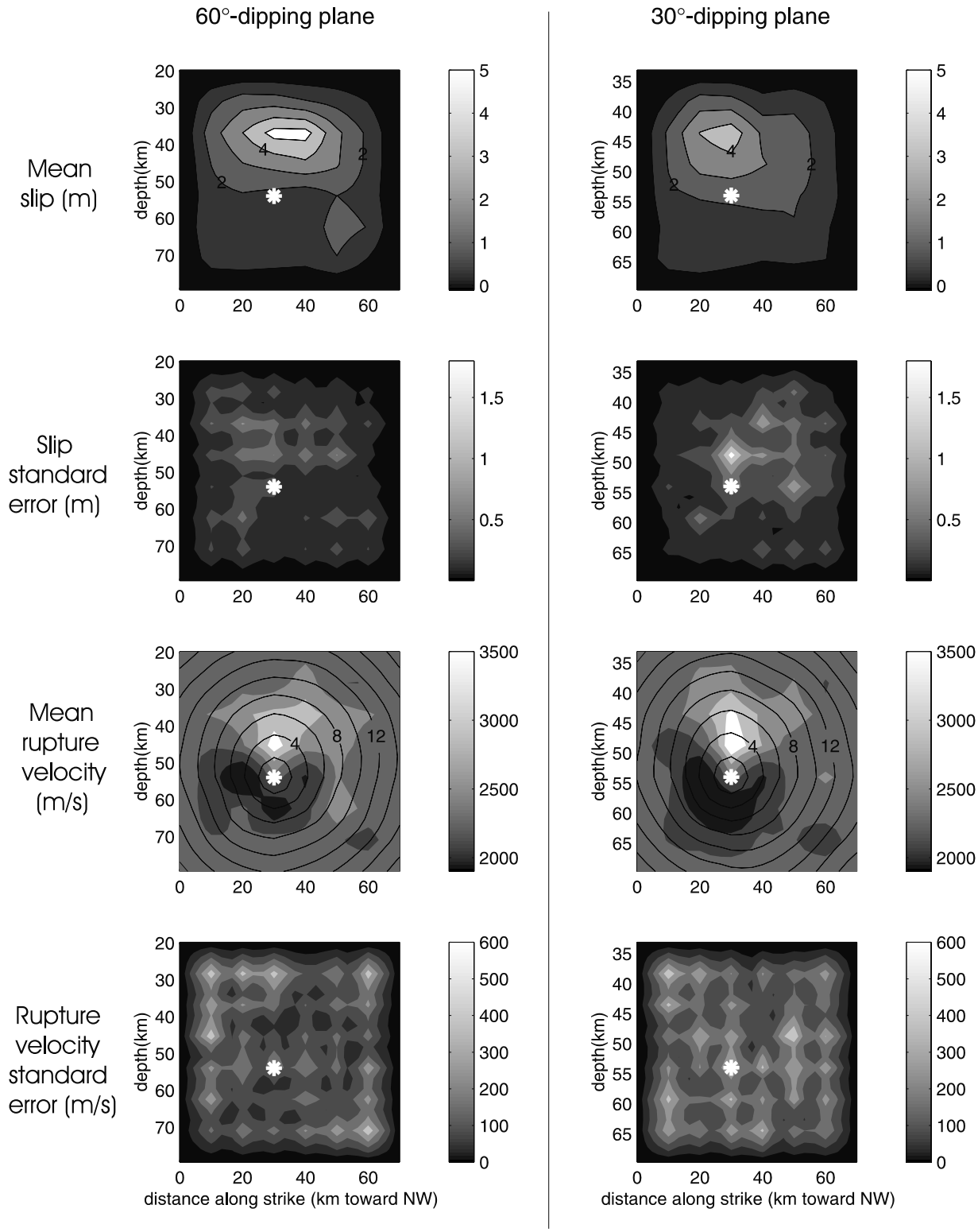

Figure 7. Mean rupture models and standard errors as in Figure 6. The slip standard error and rupture velocity error are contoured at 0.3 m and 100 m s^{-1} intervals.

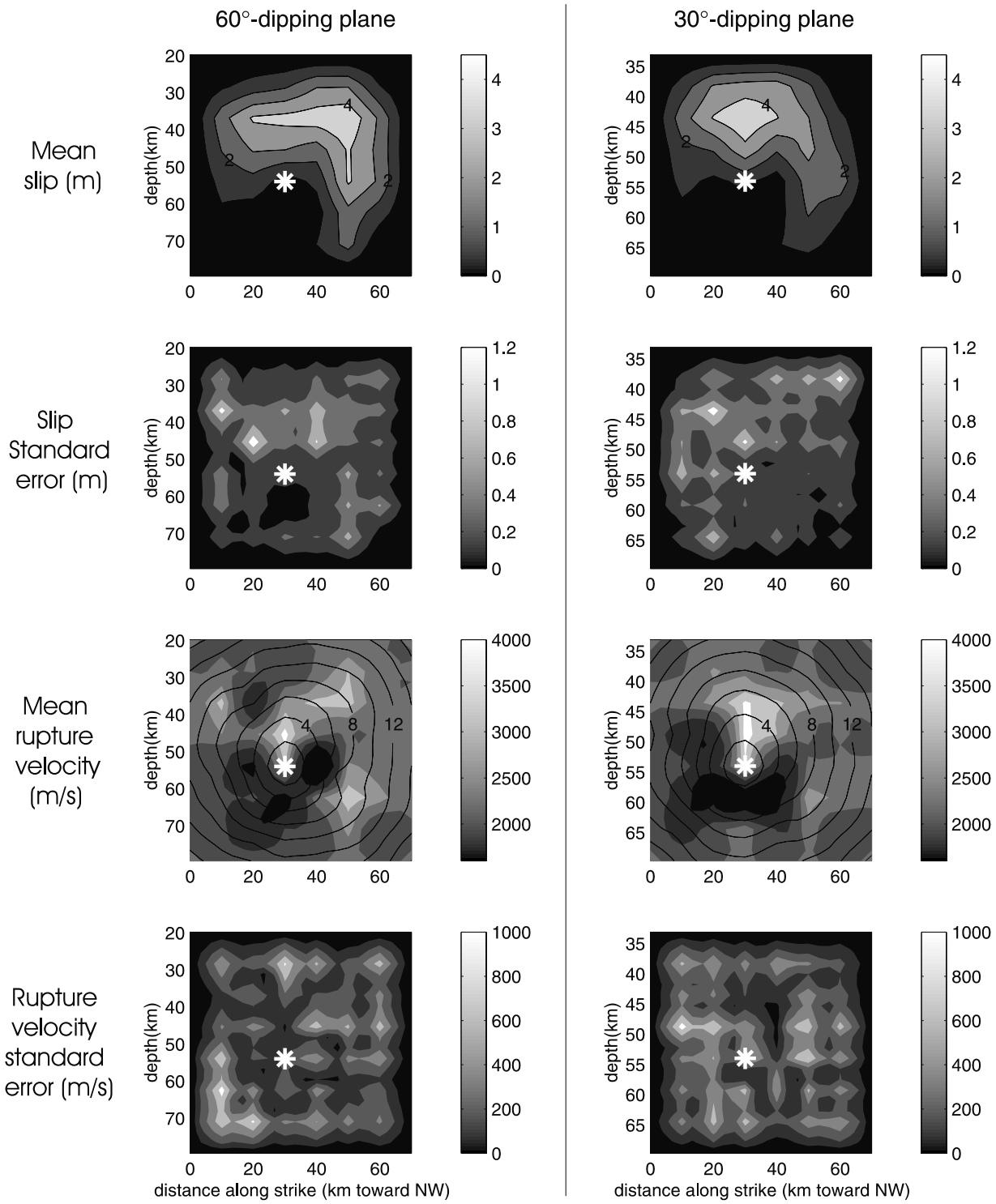

Figure 8. Rupture models obtained using only *P* and *SH* waves. As in Figure 7, but slip is contoured every 1 m, rupture velocity is contoured every 400 m s^{-1}, slip standard error is contoured every 0.3 m, and rupture velocity standard error is contoured every 200 m s^{-1}.

tion of the resulting models from independent data will significantly improve our confidence in them.

3.1. Regional Data

[32] The presence of broadband stations a few hundred kilometers from the source allows us to investigate the earthquake rupture using regional data. We use the two closest stations of the IRIS and GEOSCOPE networks, HDC in Heredia, Costa Rica, and TEIG, in Yucatan, Mexico, located at distances of 620 and 815 km from the hypocenter, respectively. We modeled the recorded ground displacements at these two locations with the discrete wave

Table 4. Source Crustal Structure Used in the Regional Study[a]

Thickness, m	V_p, m s^{-1}	V_s, m s^{-1}	ρ, kg m^{-3}	Q_p	Q_s
7000	5000	2887	2450	200	100
7000	5700	3291	2650	500	200
10000	6000	3464	2750	500	200
7000	6600	3811	2900	500	200
15000	7000	4041	3000	500	200
0	8000	4619	3330	800	400

[a]From *Ligorria and Molina* [1997].

number method [*Bouchon*, 1981], assuming the regional crustal model of *Ligorria and Molina* [1997] (Table 4). This model, obtained in Guatemala, is similar to those obtained in Chiapas, Mexico [*Castro*, 1980] and northern Costa Rica [*Matumoto et al.*, 1977] and therefore seems to be a good approximation of the crust at a regional scale. The two preferred models shown in Figure 6 were successively tested and the results are presented in Figure 9. Although these two stations are at different azimuths from the source, at these distances the waveforms are very similar for both source models and fit the data equally well. Thus the regional data cannot discriminate between the two possible rupture planes.

3.2. Near-Field Data

[33] *Universidad Centro Americana* (*UCA*) [2001] [also *Bommer et al.*, 1997] has accelerometers in El Salvador which recorded this earthquake allowing us to test our source models with near-field data. The geographic distribution of the stations is shown in Figure 10. The stations span an azimuthal range between 328° and 9° from the source and are located at distances between 67 and 109 km. As in the regional data analysis, we used the discrete wave number method to compute synthetic waveforms, but with the local crustal model used in the teleseismic inversion (Table 2). Figure 11 shows the fit comparison between the vertical component data and synthetics computed using the two fault models. Data and synthetics have both been low-pass filtered at 6 s. Unfiltered data and synthetics are also shown for the two least noisy stations, NOO and ZAO on the right of Figure 11. The fit between data and synthetics is noticeably better for the 60° dipping fault plane (bottom synthetics in Figure 11). The main pulse amplitude is too

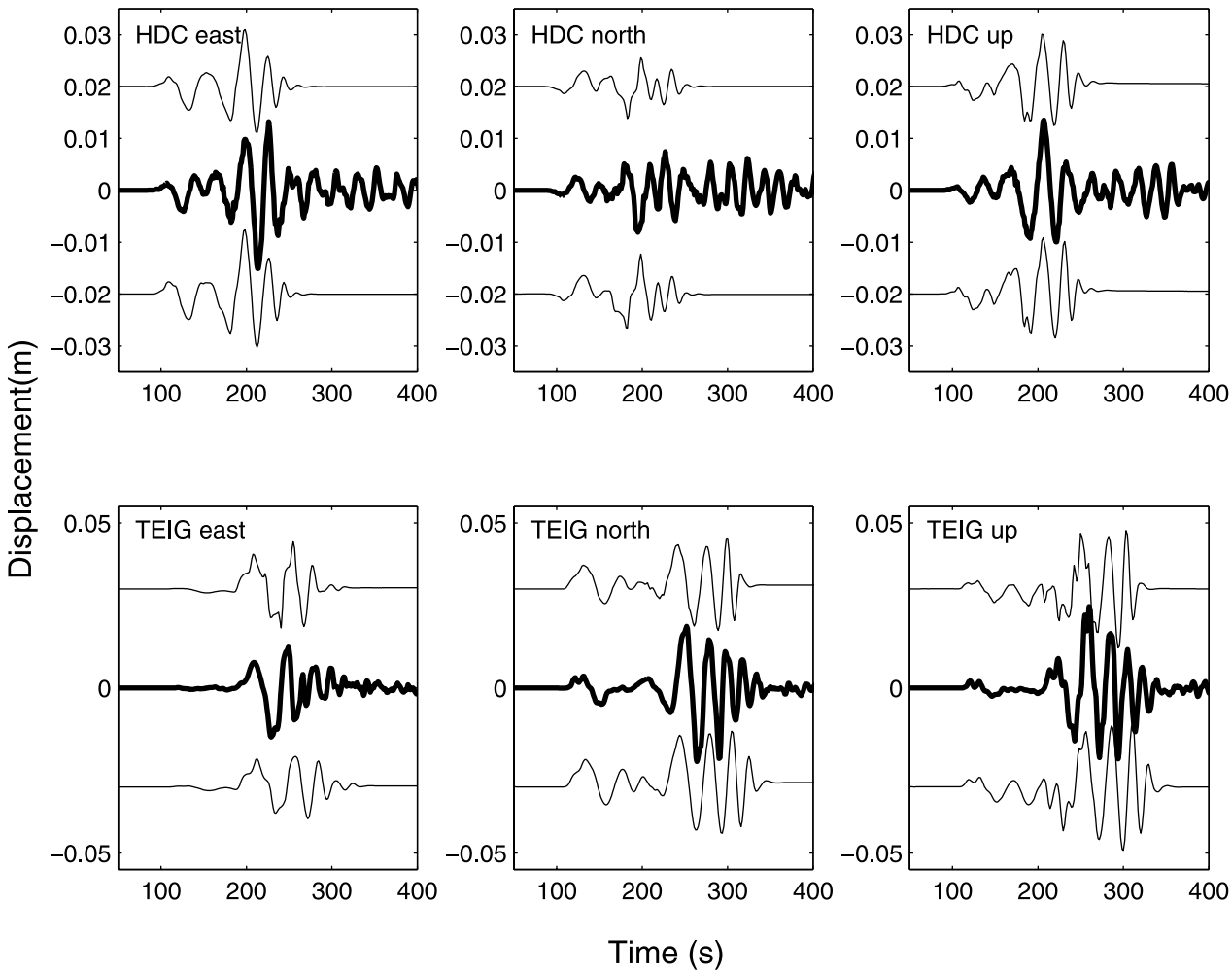

Figure 9. Model fits to three-component regional data. Thick lines are the data, and thin lines beneath the waveforms are obtained with the 60° dipping plane, while thin lines above the waveforms are obtained with the 30° dipping plane.

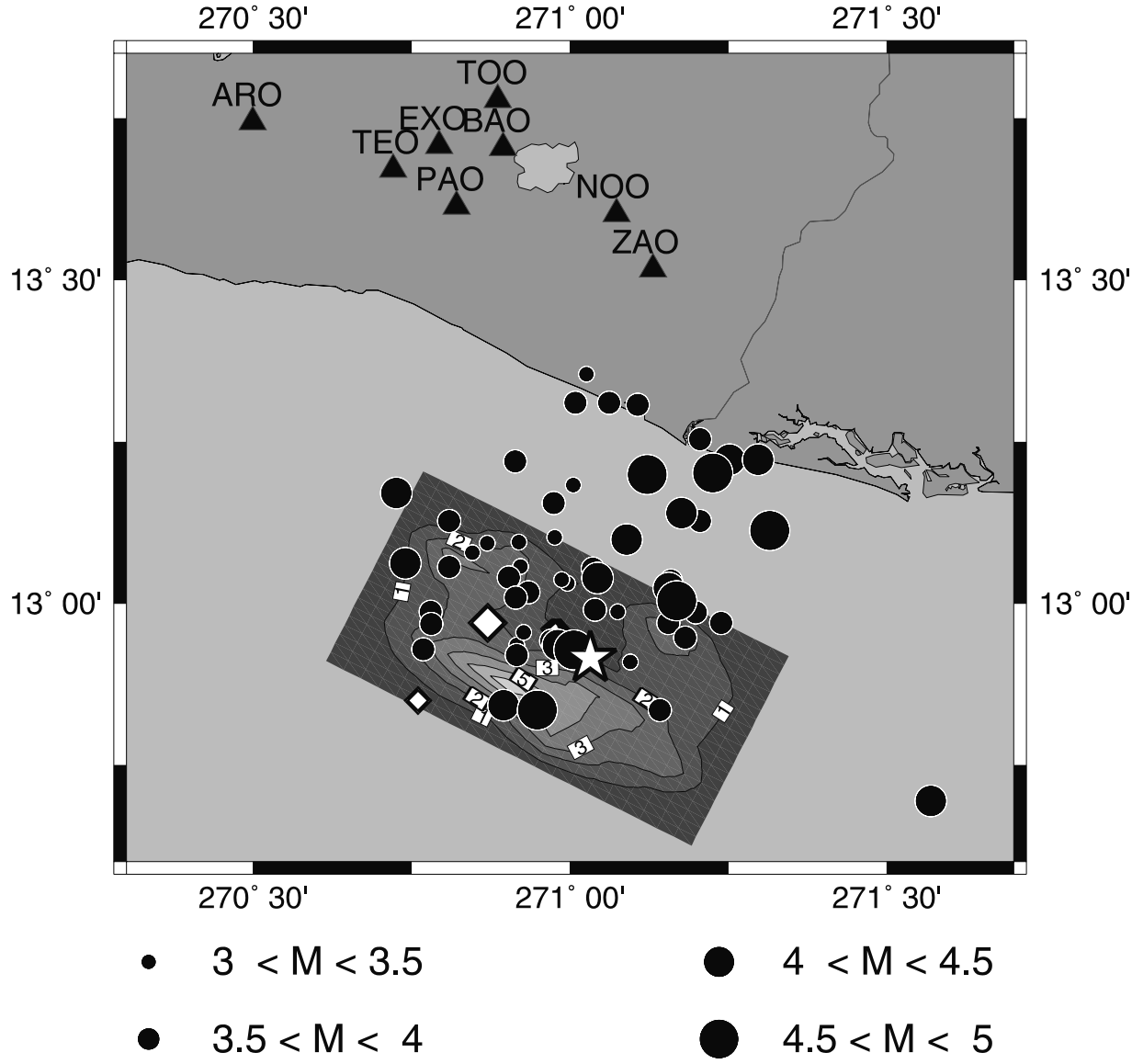

Figure 10. Location of the near-field accelerometer stations (triangles), the main shock slip distribution obtained for the 60° dipping fault plane projected onto the surface, and the main shock and 10 day aftershock locations determined by CIG. Although many of the aftershocks probably occur off the main shock fault plane, few aftershocks appear to occur in the region of concentrated main shock slip.

high at stations NOO and ZAO for the 30° dipping fault plane. This can be simply understood since both fault plane models yield mainly updip rupture propagation which is precisely in the coastal direction toward stations NOO and ZAO for the 30° dipping fault plane. On the contrary, updip propagation on the 60° dipping fault results in a lower directivity effect at near-field stations and agrees better with the observations. The slightly broader pulse for this plane compared to the observations may result from the rupture model being derived from teleseismic data on a relatively broad grid. Thus it is not surprising that our solution is less impulsive than the observed near-field data.

[34] A secondary pulse is clearly visible in the observed waveforms at ~40 s. This arrival is apparent in the 60° dipping fault model synthetics but absent in the 30° dipping fault model synthetics. Synthetics computed in a half-space velocity model for either fault dip do not contain this pulse. We believe that this pulse results from interactions with the Moho discontinuity (at 35–40 km depth) and this structural effect is more pronounced for the 60° dipping fault model.

4. Discussion and Conclusion

[35] Analysis of both teleseismic and local data provides evidence that the 13 January 2001 El Salvador earthquake occurred on a 60° dipping plane plunging toward Central America. Our preferred fault plane with strike, dip, and rake of 297°, 58°, −93° respectively, is consistent with the Harvard CMT or ERI determinations but our centroid depth is shallower, around 47 km. We find that little rupture occurred above 25 km depth, which is consistent with both the intraplate nature of this event and the very weak or even absent tsunami observed in the Pacific Ocean [*Bommer et al.*, 2002]. Rupture propagated mostly updip and toward the

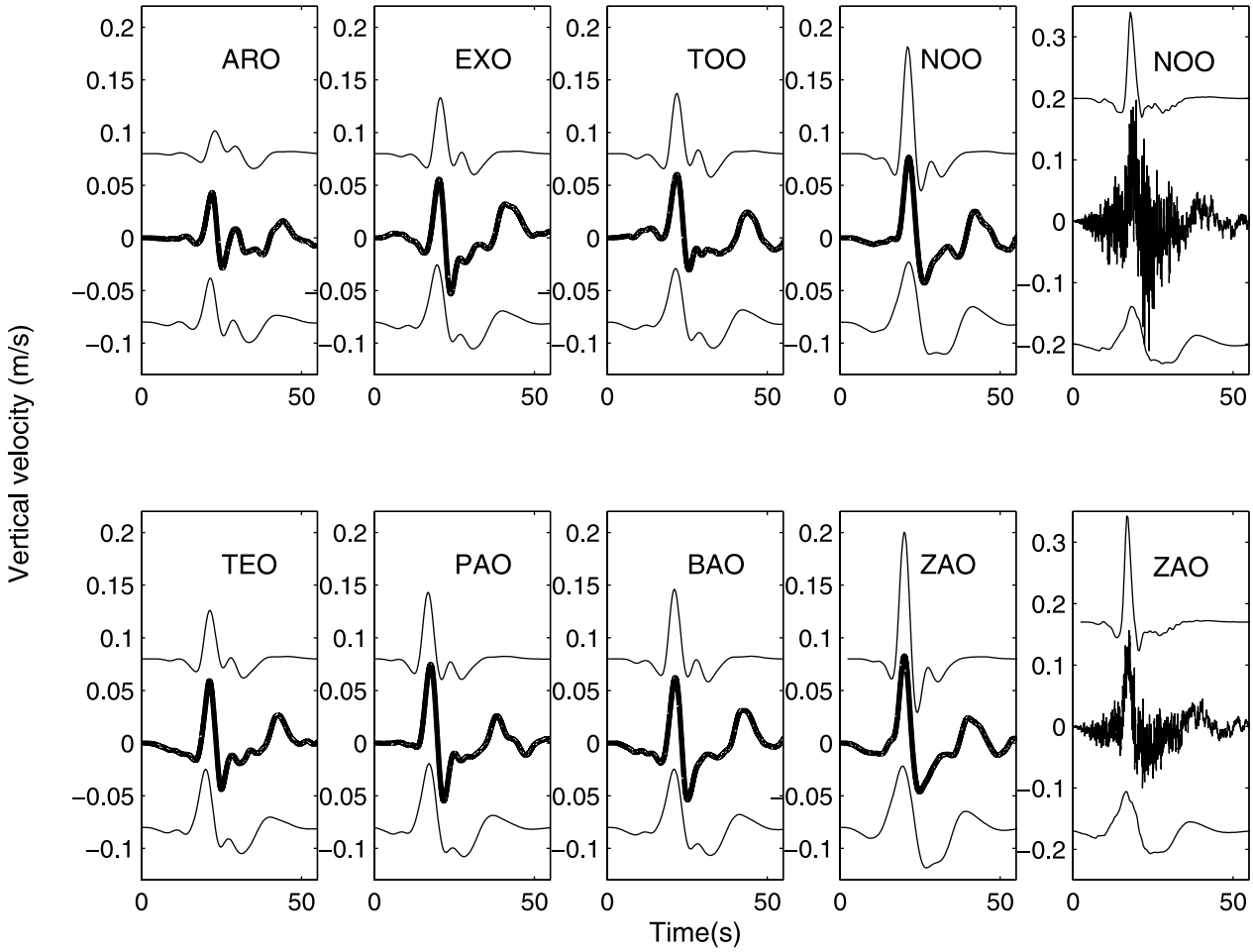

Figure 11. Model fits to near field data. Thick lines are the data, and thin lines beneath the waveforms are obtained with the 60° dipping plane, while the thin lines above the waveforms are obtained with the 30° dipping plane. Data and synthetics are low-pass filtered at 6 s except for the two seismograms on the right which have not been filtered.

northwest resulting in a 50 km wide by 25 km along-dip zone of high moment release (Figure 6). Average and maximum slip are 3.5 and 6 m, respectively, which yields a relatively high stress drop of ~130 bars. The rupture velocity clusters around 3–3.5 km s^{-1} on the majority of the rupture plane, a typical sub-Rayleigh value (0.7–0.8V_s). Moreover, we have estimated a low standard error on this parameter, around 200 m s^{-1}. This kinematic model has some similarities to the one reported by *ERI* [2001], but our inclusion of surface waves has shown that the large northwest rupture propagation of their model is unlikely.

[36] In map view the aftershocks appear to cover the entire northwest-southeast lateral extent of the earthquake rupture zone (Figure 10) but extend much farther down dip than the along-dip rupture extent. Relatively few aftershocks fall within the region of maximum slip (>3 m), and the CMT location of the EGF relative to the main shock (Figure 10) occupies a conspicuous region of no aftershock activity. Although this seems to suggest that regions of the fault plane having slipped in previous events tend to experience little subsequent slip, the quality of the aftershock locations may not be high enough to make a meaningful comparison with the main shock slip distribution. Figure 1c shows that the aftershocks scatter considerably in cross-sectional view, and it is difficult to identify a single steeply dipping fault plane from the aftershock pattern. Therefore it is impossible to discriminate between aftershocks that do and do not occur on the fault plane. Our relative location of the EGF (22 July 1996) is 3 km north and 14 km west of the main shock, placing it in the region of main moment release for the main shock; however, its depth places it 15 km below this zone and off the main shock fault plane.

[37] We find that the combination of body waves and surface waves to determine the source process is very effective because these two data sets are complementary; body waves are more sensitive to the vertical extent of the rupture while surface waves are more sensitive to its lateral extent. These data sets allowed us to define the source process of the El Salvador event without imposing many constraints on the kinematic parameters. In particular, slip and rupture velocity were completely free to vary between reasonable bounds. Confidence in our preferred model is improved by the fact that we used different data (*P* waves, *SH* waves, surface waves), different approaches (theoretical Green function, empirical Green function), and regional and

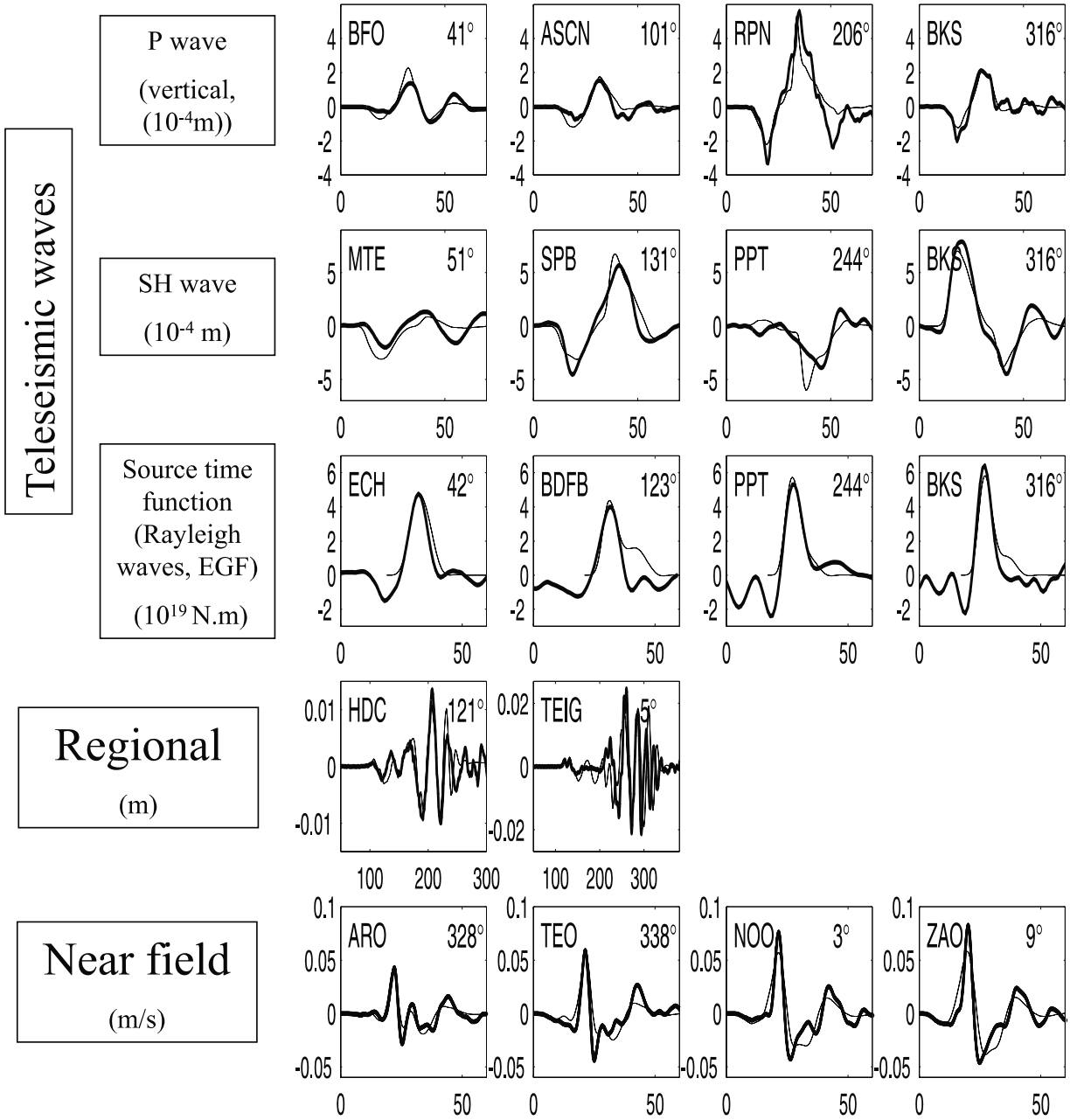

Figure 12. Synthesis of data used in this study and their fit to our preferred 60° dipping plane rupture model. Thick lines are the data, and thin lines are the synthetics. Azimuths of the stations are presented in the top right corner of each seismogram.

near-field data, even more sensitive to source effects, and obtained consistent results. In cases like the El Salvador event, where rupture is very concentrated, near field data (even one accelerometer) are very useful to confirm the actual fault plane. Figure 12 sums up the main data we modeled in this study and illustrates how well each fits our preferred kinematic source model (Figure 6) at stations located at various azimuths and distances.

[38] Tectonically, the updip rupture propagation, which yields large slip very near the plate interface (Figure 13) is consistent with a "bending event" hypothesis. In fact, the vicinity of the plate interface is the location of maximal stress in this model. Moreover, the location of background seismicity, as defined by the *Central American Seismological Center* (*CASC*) (Base de datos, 2001, available at ftp 163.178.105.34) catalog for El Salvador, shows that there is a dip increase of the subducting plate precisely at the place where the earthquake occurred (Figure 13). Observation of Figure 13 shows that there are some mislocated events (the 33 km depth lines), but unfortunately, we have no information about different location qualities to be able to select only the best located events. Yet, even with this far-from-perfect background seismicity, the bend of the slab is clearly visible and the two seismicity zones (volcanic and subduction) can be well differentiated. The steepening of the dip was already reported by *Burbach and Frohlich* [1984] in

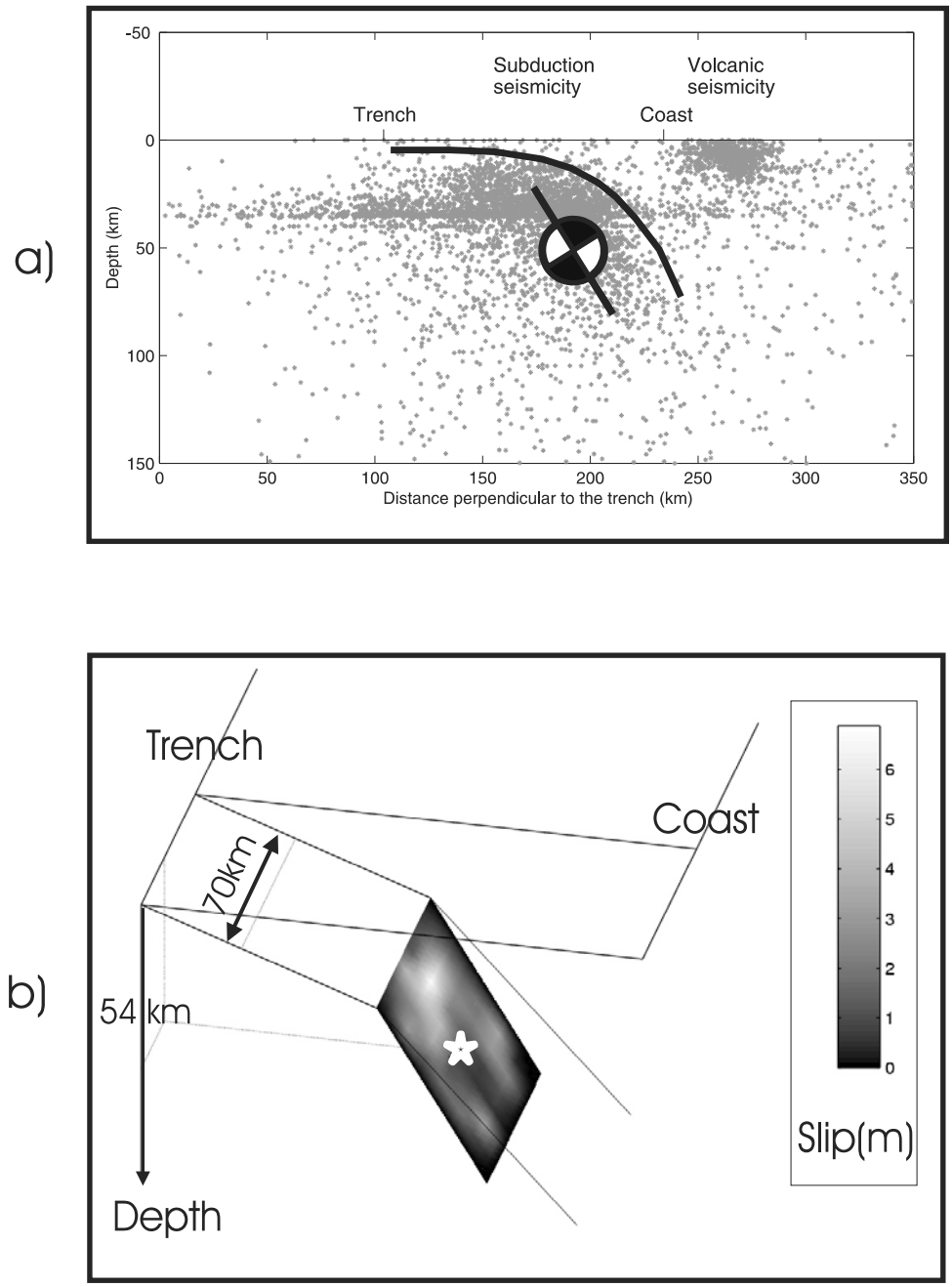

Figure 13. Tectonic interpretation of the earthquake. (a) Cross section perpendicular to the strike showing seismicity recorded by CASC in El Salvador between 1996 and 2000, and the fault plane defined by this study. The bending of the subducting plate is schematically shown by a thick line. (b) Perspective map view of the slip distribution associated with the earthquake, schematically illustrating the tectonic features of the subduction zone. The dip of the subducting plate increases at the location of the main moment release zone. See color version of this figure at back of this issue.

different parts of Central America and particularly in El Salvador. This characteristic locally increases the bending stress of the slab and has been logically shown to be a high activity zone for tensional events. Two other purely normal faulting events occurred almost in the same place in 1982 (M_w = 7.2) and 1996 (M_w = 5.6) [*Peyrat*, 1997]. *Lemoine* [2001] has shown that the correspondence between a dip increase and tensional events is often observed in other subduction zones. Our interpretation of this event is illustrated in Figure 13b: the earthquake nucleates in a moderately stressed region, inside the slab, propagates updip toward the plate interface, where the maximum slip occurred due to the large bending stresses. If "slab pull" were the dominant mechanism responsible for this event, we might expect a complete decoupling of the subducting plate since this would create a roughly homogeneous tension in the whole slab. Given the small rupture area and the slip concentration near the plate interface, this hypothesis seems

unlikely. Yet, if only the upper part of the subducting slab is brittle, as proposed, for instance, by *Spence* [1986] to explain the Sumba event (1977), the slab pull tectonic interpretation remains possible.

[39] **Acknowledgments.** We thank Malcolm Sambridge for providing us with the Neighborhood Algorithm code and Pascal Podvin for providing us with the finite difference scheme relative to the method described by *Podvin and Lecomte* [1991]. We are grateful to the IRIS, Geoscope, and NCEDC networks from which we retrieved the worldwide recordings of the earthquake and to Universidad CentroAmericana for the free access to the accelerograms. We thank Jocelyn Guilbert, Bruno Feignier, Anne Lemoine, and André Herrero for discussions. Finally, we thank the two anonymous referees who helped to improve the final version of this article. This work was supported by a grant from the Centre National de la Recherche Scientifique (CNRS) and from the Commissariat a l'Energie Atomique (CEA/DASE).

References

Astiz, L., and H. Kanamori, Interplate coupling and temporal variation of mechanisms of intermediate-depth earthquakes in Chile, *Bull. Seismol. Soc. Am.*, *83*, 811–829, 1986.

Bilek, S., and T. Lay, Variation of interplate fault zone properties with depth in the Japan subduction zone, *Science*, *281*, 1175–1178, 1998.

Bommer, J. J., et al., A new digital accelerograph network for El Salvador, *Seismol. Res. Lett.*, *68*, 426–437, 1997.

Bommer, J. J., et al., The El Salvador earthquakes of January and February 2001: Context, characteristics and implications for seismic risk, *Soil Dyn. Earthquake Eng.*, *22*, 389–418, 2002.

Bouchon, M., Teleseismic body wave radiation from a seismic source in a layered medium, *Geophys. J. R. Astron. Soc.*, *47*, 515–530, 1976.

Bouchon, M., A simple method to calculate Green's functions for elastic layered media, *Bull. Seismol. Soc. Am.*, *71*, 959–971, 1981.

Burbach, G., and C. Frohlich, Seismicity and tectonics of the subducted Cocos Plate, *J. Geophys. Res.*, *89*, 7719–7735, 1984.

Castro, R. R., Un modelo de la corteza terrestre para el sur de Mexico mediante el uso de sismos pro-fundos, thesis, 75 pp., Fac. de Ing., Univ. Nac. Automata Mexico, 1980.

Central American Seismological Center (CASC), Base de datos, *ftp 163.178.105.34.*, 2001.

Christensen, D. H., and T. Lay, Large earthquakes in the Tonga region associated with subduction of the Louisville Ridge, *J. Geophys. Res.*, *93*, 13,367–13,389, 1988.

Christensen, D. H., and L. J. Ruff, Seismic coupling and outer rise earthquakes, *J. Geophys. Res.*, *93*, 13,421–13,444, 1988.

Cocco, M., J. Pacheco, S. K. Singh, and F. Courboulex, The Zihuatanejo, Mexico, earthquake of 1994 December 10 (M = 6.6): Source characteristics and tectonic implications, *Geophys. J. Int.*, *131*, 135–145, 1997.

Cotton, F., and M. Campillo, Frequency domain inversion of strong motions: Application to the 1992 Landers earthquake, *J. Geophys. Res.*, *100*, 3961–3975, 1995.

Courboulex, F., S. K. Singh, J. F. Pacheco, and C. J. Ammon, The 1995 Colima-Jalisco, Mexico, earthquake (M_w 8): A study of the rupture process, *Geophys. Res. Lett.*, *24*, 1019–1022, 1997.

Dmowska, R., and L. C. Lovison, Influence of asperities along subduction interfaces on the stressing and seismicity of adjacent areas, *Tectonophysics*, *211*, 23–43, 1992.

Earthquake Research Institute (ERI), EIC seismological note: El Salvador Earthquake on January 13, 2001, Univ. of Tokyo, Tokyo, 2001.

Ekström, G., A very broad band inversion method for the recovery of earthquake source parameters, *Tectonophysics*, *166*, 73–100, 1989.

Eshelby, J. D., The determination of the elastic field of an ellipsoidal inclusion and related problems, *Proc. R. Soc. London, Ser. A*, *241*, 376–396, 1957.

Given, J. W., and H. Kanamori, The depth extent of the 1977 Sumbawa, Indonesia earthquake, *Eos Trans. AGU*, *61*, 1044, 1980.

Hartzell, S. H., and T. H. Heaton, Inversion of strong ground motion and teleseismic waveform data for the fault rupture history of the 1979 Imperial Valley, California, earthquake, *Bull. Seismol. Soc. Am.*, *73*, 1553–1583, 1983.

Hartzell, S. H., and P. Liu, Calculation of earthquake rupture histories using a hybrid global search algorithm: Application to the 1992 Landers, California, earthquake, *Phys. Earth PLanet. Inter.*, *95*, 79–99, 1996.

Hartzell, S. H., G. S. Stewart, and C. Mendoza, Comparison of L_1 and L_2 norms in a teleseismic waveform inversion for the slip history of the Loma Prieta, California, earthquake, *Bull. Seismol. Soc. Am.*, *81*, 1518–1539, 1991.

Hernandez, B., N. M. Shapiro, S. K. Singh, J. F. Pacheco, F. Cotton, M. Campillo, A. Iglesias, V. Cruz, J. M. Gomez, and L. Alcantara, Rupture history of September 30, 1999 intraplate earthquake of Oaxaca, Mexico (M_w = 7.5) from inversion of strong-motion data, *Geophys. Res. Lett.*, *28*, 363–366, 2001.

Herrero, A., Space-time and spectral parameterisation of seismic sources and its application to seismic hazard, Ph.D. thesis, Inst. de Phys. du Globe Paris, Paris, France, 1994.

Houston, H., Influence of depth, focal mechanism, and tectonic setting on the shape and duration of earthquake source time functions, *J. Geophys. Res.*, *106*, 11,137–11,350, 2001.

Ihmle, P. F., On the interpretation of subevents in teleseismic waveforms: The 1994 Bolivia deep earthquake revisited, *J. Geophys. Res.*, *103*, 17,919–17,932, 1998.

Kanamori, H., and D. L. Anderson, Theoretical basis of some empirical relations in seismology, *Bull. Seismol. Soc. Am.*, *65*, 1073–1095, 1975.

Kausel, E., and J. Campos, The M_s = 8 tensional earthquake of 9 December 1950 of northern Chile and its relation to the seismic potential of the region, *Phys. Earth Planet. Inter.*, *72*, 220–235, 1992.

Kennett, B. L. N., K. Marson-Pidgeon, and M. S. Sambridge, Seismic source characterization using a neighbourhood algorithm, *Geophys. Res. Lett.*, *27*, 3401–3404, 2000.

Kim, J. J., T. Matumoto, and G. V. Latham, A crustal section of northern Central America as inferred from wide-angle reflections from shallow earthquakes, *Bull. Seismol. Soc. Am.*, *72*, 925–940, 1982.

Lay, T., L. Astiz, H. Kanamori, and D. H. Christensen, Temporal variation of large intraplate earthquakes in subduction zones, *Phys. Earth Planet. Inter.*, *54*, 258–312, 1989.

Lemoine, A., Grands séismes intraplaques en Amérique du Sud et en Amérique Centrale, thèse de l'Univ. Paris Sud, Orsay, France, 2001.

Ligorria, J. P., and E. Molina, Crustal velocity structure of southern Guatemala using refracted and *Sp* converted waves, *Geofis. Int.*, *36*, 1, 1997.

Lomax, A., and R. Snieder, Finding sets of acceptable solutions with a genetic algorithm with application to surface wave group dispersion in Europe, *Geophys. Res. Lett.*, *21*, 2617–2620, 1994.

Lundgren, P. R., and E. A. Okal, Slab decoupling in the Tonga arc: The June 22, 1977, earthquake, *J. Geophys. Res.*, *93*, 13,355–13,366, 1988.

Lynnes, C. S., and T. Lay, Source process of the great 1977 Sumba earthquake, *J. Geophys. Res.*, *93*, 13,407–13,420, 1988.

Marson-Pidgeon, K., B. L. N. Kennett, and M. Sambridge, Source depth and mechanism inversion at teleseismic distances using a neighborhood algorithm, *Bull. Seismol. Soc. Am.*, *90*, 1369–1383, 2000.

Matumoto, T., M. Ohtake, G. Latham, and J. Umana, Crustal structure in southern Central America, *Bull. Seismol. Soc. Am.*, *67*, 121–134, 1977.

Mendoza, C., S. Hartzell, and T. Monfret, Wide-band analysis of the 3 March 1985 central Chile earthquake: Overall source process and rupture history, *Bull. Seismol. Soc. Am.*, *84*, 269–283, 1994.

Mikumo, T., S. K. Singh, and M. A. Santoyo, A possible stress interaction between large thrust and normal-faulting earthquakes in the Mexican subduction zone, *Bull. Seismol. Soc. Am.*, *89*, 1418–1427, 1999.

Mikumo, T., Y. Yagi, S. K. Singh, and M. A. Santoyo, Coseismic and postseismic stress changes in a subducting plate: Possible stress interactions between large interplate thrust and intraplate normal-faulting earthquakes, *J. Geophys. Res.*, *107*(B1), 2023, doi:10.1029/2001JB000446, 2002.

Mohammadioun, B., and L. Serva, Stress drop, slip type, earthquake magnitude, and seismic hazard, *Bull. Seismol. Soc. Am.*, *91*, 694–707, 2001.

Mooney, W. D., G. Laske, and T. G. Masters, CRUST 5.1: A global crustal model at 5° × 5°, *J. Geophys. Res.*, *103*, 727–747, 1998.

Nelder, J. A., and R. Mead, A simplex method for function minimization, *Comput. J.*, *7*, 308–313, 1965.

Peyrat, S., Etude du séisme du 22/07/1996 au Salvador, Diplome d'études approfondies, 35 pp., Lab. Terre-Atmos.-Ocean, Ecole Normale Supérieure, Paris, 1997.

Pho, T. P., and L. Behe, Extended distances and angles of incidence of *P* waves, *Bull. Seismol. Soc. Am.*, *62*, 885–902, 1972.

Podvin, P., and I. Lecomte, Finite difference computation of traveltimes in very contrasted velocity models: A massively parallel approach and its associated tools, *Geophys. J. Int.*, *105*, 271–284, 1991.

Ratchkovski, N. A., and R. A. Hansen, Sequence of strong intraplate earthquakes in the Kodiak Island region, Alaska in 1999–2001, *Geophys. Res. Lett.*, *28*, 3729–3732, 2001.

Sambridge, M., Geophysical inversion with a neighbourhood algorithm. I. Searching a parameter space, *Geophys. J. Int*, *138*, 479–494, 1999.

Scholz, C. H., C. A. Aviles, and S. G. Wesnousky, Differences between interplate and intraplate earthquakes, *Bull. Seismol. Soc. Am.*, *76*, 65–70, 1986.

Schwartz, S. Y., Noncharacteristic behavior and complex recurrence of large subduction zone earthquakes, *J. Geophys. Res.*, *104*, 23,111–23,125, 1999.

Singh, S. K., et al., The Oaxaca earthquake of September 30, 1999 (M_w = 7.5): A normal-faulting event in the subducted Cocos plate, *Seismol. Res. Lett.*, *71*, 67–78, 2000.

Spence, W., The 1977 Sumba earthquake series: Evidence for slab pull force acting at a subduction zone, *J. Geophys. Res.*, *91*, 7225–7239, 1986.

Takeo, M., S. Ide, and Y. Yoshida, The 1993 Kushiro-Oki, Japan, earthquake: A high stress–drop event in a subducting slab, *Geophys. Res. Lett.*, *20*, 2607–2610, 1993.

Universidad Centro Americana (UCA), Strong motion data form the January–February earthquakes in El Salvador, report, San Salvador, El Salvador, 2001.

Velasco, A. A., C. J. Ammon, and T. Lay, Recent large earthquakes near Cape Mendocino and in the Gorda plate: Broadband source time functions, fault orientations, and rupture complexities, *J. Geophys. Res.*, *99*, 711–728, 1994a.

Velasco, A. A., C. J. Ammon, and T. Lay, Empirical Green function deconvolution of broadband surface waves: Rupture directivity of the 1992 Landers, California (M_w = 7.3), *Bull. Seismol. Soc. Am.*, *84*, 735–750, 1994b.

Walther, C. H. E., E. R. Flueh, C. R. Ranero, R. Von-Huene, and W. Strauch, Crustal structure across the Pacific margin of Nicaragua: Evidence for ophiolitic basement and a shallow mantle sliver, *Geophys. J. Int.*, *141*, 759–777, 2000.

Wells, D. L., and K. J. Coppersmith, New empirical relationships among magnitude, rupture length, rupture width, rupture area, and surface displacement, *Bull. Seismol. Soc. Am.*, *84*, 974–1002, 1994.

Wiens, D. A., Bathymetric effects on body waveforms from shallow subduction zone earthquakes and application to seismic processes in the Kurile trench, *J. Geophys. Res.*, *94*, 2955–2972, 1989.

M. Bouchon and M. Vallée, LGIT, BP 53X, F-38041 Grenoble, France. (mvallee@obs.ujf-grenoble.fr)

S. Y. Schwartz, Earth Sciences Department, University of California, Santa Cruz, 1156 High Street, Santa Cruz, CA 95064-1077, USA. (sschwartz@es.ucsc.edu)

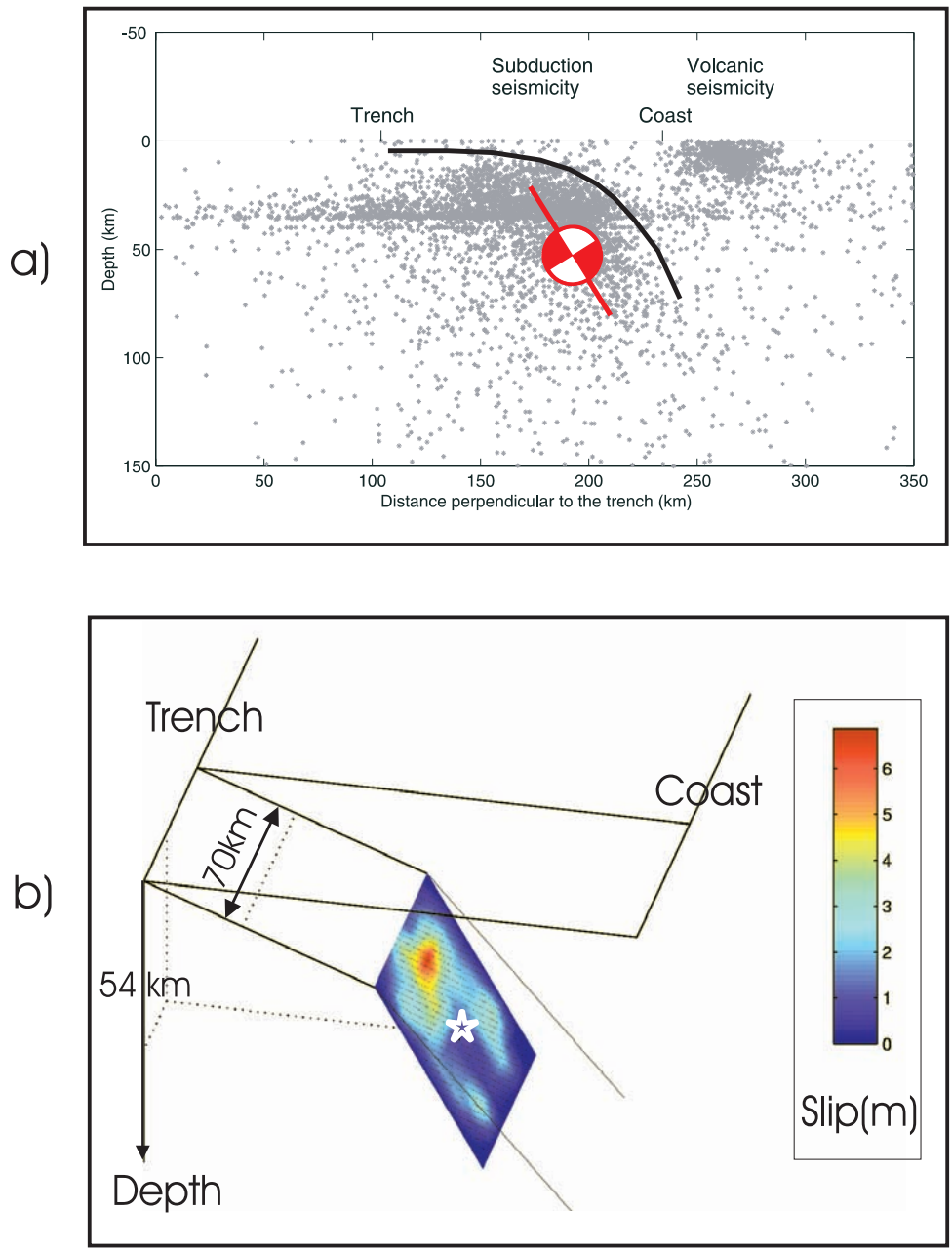

Figure 13. Tectonic interpretation of the earthquake. (a) Cross section perpendicular to the strike showing seismicity recorded by CASC in El Salvador between 1996 and 2000, and the fault plane defined by this study. The bending of the subducting plate is schematically shown by a thick line. (b) Perspective map view of the slip distribution associated with the earthquake, schematically illustrating the tectonic features of the subduction zone. The dip of the subducting plate increases at the location of the main moment release zone.